NOTE TO USERS

This reproduction is the best copy available.

UMI®

Reproduced with permission of the copyright owner. Further reproduction prohibited without permission.

Reproduced with permission of the copyright owner. Further reproduction prohibited without permission.

University of Alberta

Microscopy and Spectroscopy of Pentacene Thin Films

by

Hui Qian

A thesis submitted to the Faculty of Graduate Studies and Research in partial fulfillment of the requirements for the degree of

Master of Science

Department of Physics

Edmonton, Alberta

Fall 2005

Reproduced with permission of the copyright owner. Further reproduction prohibited without permission.

Library and Archives Canada

Published Heritage Branch

395 Wellington Street
Ottawa ON K1A 0N4
Canada

Bibliothèque et Archives Canada

Direction du Patrimoine de l'édition

395, rue Wellington
Ottawa ON K1A 0N4
Canada

Your file Votre référence
ISBN: 0-494-09270-X
Our file Notre référence
ISBN: 0-494-09270-X

NOTICE:
The author has granted a non-exclusive license allowing Library and Archives Canada to reproduce, publish, archive, preserve, conserve, communicate to the public by telecommunication or on the Internet, loan, distribute and sell theses worldwide, for commercial or non-commercial purposes, in microform, paper, electronic and/or any other formats.

The author retains copyright ownership and moral rights in this thesis. Neither the thesis nor substantial extracts from it may be printed or otherwise reproduced without the author's permission.

AVIS:
L'auteur a accordé une licence non exclusive permettant à la Bibliothèque et Archives Canada de reproduire, publier, archiver, sauvegarder, conserver, transmettre au public par télécommunication ou par l'Internet, prêter, distribuer et vendre des thèses partout dans le monde, à des fins commerciales ou autres, sur support microforme, papier, électronique et/ou autres formats.

L'auteur conserve la propriété du droit d'auteur et des droits moraux qui protège cette thèse. Ni la thèse ni des extraits substantiels de celle-ci ne doivent être imprimés ou autrement reproduits sans son autorisation.

In compliance with the Canadian Privacy Act some supporting forms may have been removed from this thesis.

While these forms may be included in the document page count, their removal does not represent any loss of content from the thesis.

Conformément à la loi canadienne sur la protection de la vie privée, quelques formulaires secondaires ont été enlevés de cette thèse.

Bien que ces formulaires aient inclus dans la pagination, il n'y aura aucun contenu manquant.

Reproduced with permission of the copyright owner. Further reproduction prohibited without permission.

Abstract

Pentacene is one of the most important semiconductor materials used in organic electronics. In this thesis, growth of pentacene thin films on various substrates, their properties, morphology and microstructure were studied by transmission electron microscopy (TEM), X-ray diffraction (XRD), atomic force microscopy (AFM) and various optical spectroscopies. The evolution of thin film growth by vacuum thermal evaporation from sub-monolayer (ML) to more than 70 nm was studied by TEM and AFM. It was found that during the early stage, the growth mode changes from two-dimensional (2D) to three-dimensional (3D) at about one ML thickness. The transition in growth mode is accompanied by a dramatic change in film morphology. Different 2D islands (dendritic- and round-shaped) were obtained by varying the deposition rate. Sensitivity of pentacene thin films to electron beam irradiation in an analytical TEM was measured at both room temperature and 90 K, based on the loss of film crystallinity and the degradation of molecular structure. Optical properties were characterized with visible and UV absorption and photoluminescence (PL) measurements.

Reproduced with permission of the copyright owner. Further reproduction prohibited without permission.

Acknowledgements

I would like to take this opportunity to thank my supervisor Dr. Ray Egerton and co-supervisor Dr. Marek Malac for academic advice, financial support, encouragement and patience during my MSc. program. This thesis would not have been possible without their technical guiding and challenge when I was lost in the jungle of experimental data. Besides being an excellent academic supervisor, Ray has also become a friend to me. I am lucky to get to know Ray and his wife Maia in my life.

I would also like to thank Dr. Al Meldrum, who had kindly offered his photoluminescence lab and his summer student Cindy Blois to help me with optical property measurements. I am grateful for Greg Popwich, who provided excellent technical help in the electron microscopy lab. My fellow graduate students Peng Li and Feng Wang are thanked for helps on radiation damage measurement in TEM and many suggestions. Also my appreciation goes to the Department of Physics for offering me a research assistant scholarship to reduce my teaching load.

Deep appreciations go to my parents and parents-in-law who had helped to look after my lovely son Daniel during my MSc. program. Last, but not least, I am deeply indebt to my husband Xianling and my son Daniel for their love, understanding and support that make this MSc. program a fruitful and happy journey.

Reproduced with permission of the copyright owner. Further reproduction prohibited without permission.

Table of Contents

CHAPTER 1. INTRODUCTION 1

1.1. Overview of Organic Thin Films 1

1.2. Pentacene Crystals 4

1.3. Characterization of Pentacene Thin Films 7

1.4. Outline of This Thesis 8

CHAPTER 2. MORPHOLOGY, STRUCTURE AND GROWTH OF PENTACENE THIN FILMS 10

2.1. Introduction 10

2.2. High Vacuum Evaporation Setup 12

2.3. Crystallographic Orientation of Pentacene Thin Films 13

2.3.1. Ratio Method to Index Diffraction Patterns 14

2.3.2. Calibration of the Camera Constant in a TEM 15

2.3.3. Textured Polycrystalline Structure 20

2.4. Evolution of Pentacene Thin Film Growth 22

2.4.1. Experiment Details 22

2.4.2. Results and Discussions 23

2.5. Effect of Growth Conditions on the Morphology and Structure of Pentacene Thin Films 31

2.6. Post Deposition Annealing of the Films 37

2.7. Conclusions 38

Reproduced with permission of the copyright owner. Further reproduction prohibited without permission.

CHAPTER 3. ELECTRON RADIATION DAMAGE OF PENTACENE THIN FILMS MEASURED IN TEM 39

3.1. Introduction 39

3.2. Experimental Methods 41

3.2.1. Loss of Long-Range Order Measured by Diffraction Pattern Fading..... 42

3.2.2. Loss of Short-Range Order Measured by Electron Energy Loss Spectroscopy 44

3.3. Discussion of Experimental Results 46

3.3.1. Loss of Long-Range Order Observed in Diffraction Patterns 46

3.3.2. Loss of Short -Range Order Observed in EELS Measurement 50

3.4. Discussions of Electron-Beam-Induced Radiation Damage in Pentacene 54

CHAPTER 4: OPTICAL PROPERTIES OF PENTACENE THIN FILMS 56

4.1. Introduction 56

4.2. Optical Absorption and Photoluminescence Measurement 59

4.2.1. Experimental 59

4.2.2. Results of Absorption Measurement 59

4.2.3. Photoluminescence Measurement 62

4.3. Optical Properties Calculated from Electron-Energy Loss Spectrum 62

4.3.1. EELS Spectrum Measurement 64

4.3.2. Calculation of Optical Constants 65

CHAPTER 5. SUMMARY 67

Reproduced with permission of the copyright owner. Further reproduction prohibited without permission.

REFERENCES **70**

APPENDIX: CALCULATION OF *D* SPACING AND RATIOS OF (*HKL*)

PLANES **73**

Reproduced with permission of the copyright owner. Further reproduction prohibited without permission.

List of Tables

Table 2.1: d-spacings and corresponding reflection planes assigned for the inner 10 rings in diffraction pattern of pentacene thin films deposited at RT.

Table 2.2: Measured data from XRD of pentacene thin film deposited on C film.

Table 2.3. Measured data from XRD spectrum of pentacene thin films deposited on carbon at 40 °C. T, B mean thin film phase and bulk phase, respectively.

Table 3.1. Characteristic and end-point doses at various dose rates j measured by fading of (110) diffraction ring, both at room temperature and at 90 K.

Table 3.2. Characteristic dose $D_{1/e}$, end-point dose D_c and latent dose for each DP ring measured at 295 K and 90 K.

Table 3.3. End-point dose for fading of 8.7 eV peak, measured for pentacene at room temperature and at 90 K.

Table 3.4. Calculated damage characteristic doses per molecule.

Table 3.5. Measured damage cross-sections using the end-point dose both for DP (110), (320) plane and EELS 7 eV, 8.7 eV peak destruction.

Reproduced with permission of the copyright owner. Further reproduction prohibited without permission.

List of Figures

Figure 1.1. (a) Pentacene molecular structure and (b) bulk crystalline structure of pentacene with lattice parameters: a=7.93±0.02 Å, b=6.14±0.02 Å, c=16.03±0.05 Å, α=101.9°, β=112.6°, γ=85.8°, viewed along the [010] axis.

Figure 1.2. Mobility of p-type organic semiconductors versus time of development. (Dimitrakopoulos, 2002).

Figure 2.1. Thermal evaporation setup for pentacene thin film deposition.

Figure 2.2. Schematic diagram of a simple electron diffraction camera.

Figure 2.3. DP of pentacene thin films deposited on amorphous carbon film at RT with a thickness of 70 nm.

Figure 2.4. Indexed reciprocal lattice points for a pentacene single crystal, with incident electron beam along [001] direction.

Figure 2.5. XRD spectra of pentacene deposited on amorphous carbon film at RT with a thickness of 70 nm.

Figure 2.6. XRD spectra of pentacene deposited on Si (001) at a rate of 0.1 Å/s at RT with a thickness of 100 nm.

Figure 2.7. Diffraction patterns of pentacene films taken at a tilting angle β is 0°, 15° and 30°, respectively.

Figure 2.8. TEM images of pentacene ultra thin film formation with gradient thickness from a) to f), obtained by using shadow mask.

Reproduced with permission of the copyright owner. Further reproduction prohibited without permission.

Figure 2.9. AFM images (5 μm × 5 μm) of pentacene deposited onto carbon films using shadow mask.

Figure 2.10. TEM images of pentacene thin films formation with gradient thickness from a) to f), obtaining by varing the deposition time, with the same evaporation rate 0.1 Å/s at RT onto carbon pre-covered TEM grids.

Figure 2.11. AFM images of pentacene thin film formation with thickness gradient from a) to d), obtaining by varing the deposition time, with the same evapration rate 0.1 Å/s at RT onto glass. The size of image is 5 μm × 5 μm.

Figure 2.12. Diffraction patterns of the pentacene islands. Left: before shape change; right: after shape change.

Figure 2.13. a) AFM image (2 μm × 2 μm) of pentacene films deposited onto glass at a rate of 0.1 Å/s at RT; b) profile of one island with height of about 10 nm.

Figure 2.14. AFM image (3 μm × 3 μm) of pentacene films deposited onto mica at RT, with thickness of 70 nm.

Figure 2.15. AFM images of pentacene films deposited on amorphous carbon foil a) at 0.5 Å/s at RT; b) at 1 Å/s at RT; c) at 0.5 Å/s at 40 °C.

Figure 2.16. AFM images of surface plot of pentacene films deposited on mica at elevated temperatures.

Figure 2.17. XRD spectra of pentacene films deposited on carbon foil at substrate temperature 20°C, 40°C and 60°C, respectively.

Reproduced with permission of the copyright owner. Further reproduction prohibited without permission.

Figure 2.18. Pentacene films annealed at 190°C. Left: 30 minutes to cool to RT; right: constant temperature at 190°C for 15 minutes, then 60 minutes to cool to RT.

Figure 3.1. Crystallinity-loss as a function of irradiation dose D, for pentacene thin films irradiated at 200 kV in TEM.

Figure 3.2. Change in morphology observed in bright field images of pentacene films as a result of electron beam damage.

Figure 3.3. Diffraction pattern of polycrystalline pentacene thin films (70 nm) deposited onto amorphous carbon at RT.

Figure 3.4. Left: integrated diffraction intensity over all azimuthal angles (0°-360°) of each ring; right: corresponding integrated Digital Micrograph profile.

Figure 3.5. Peaks corresponding to (110), (200), (210), (220), (130) and (320) reflections were fitted using Lorentzian function.

Figure 3.6. π-Excitation peaks in the energy loss spectrum of pentacene.

Figure 3.7. Fading of diffraction rings monitored at room temperature with dose rate $j = 0.6\times10^{-3}$ A/cm^2.

Figure 3.8. Fading of diffraction rings with beam dose measured at liquid-nitrogen cooling temperature 90 K with dose rate $j = 4.3\times10^{-3}$ A/cm^2.

Figure 3.9. The intensity of 7 eV peak of pentacene thin films versus beam dose measured at room temperature.

Figure 3.10. Series of low-loss spectra of pentacene measured at selected time intervals.

Reproduced with permission of the copyright owner. Further reproduction prohibited without permission.

Figure 3.11. Logarithm total intensity of ZLP and plasmon region over the intensity of ZLP versus beam dose.

Figure 4.1. π-electron luminescence process (Lumb, 1978).

Figure 4.2. Measured absorption spectrum of pentacene thin films deposited onto fused quartz at RT.

Figure 4.3. Absorption spectra of pentacene films, deposited at room temperature as a function of thickness.

Figure 4.4. PL spectra of pentacene films deposited onto Si(001) wafer at RT.

Figure 4.5. Low-loss region spectrum of 70 nm thick pentacene films, deposited onto amorphous carbon at RT.

Figure 4.6. a) The dielectric constant ε_1 and ε_2 for pentacene films calculated from the energy loss function; b) the calculated optical absorption coefficient μ (E).

Reproduced with permission of the copyright owner. Further reproduction prohibited without permission.

List of Abbreviations

AFM	atomic force microscopy
AMLCD	active matrix liquid crystal display
CMOS	complementary metal oxide semiconductor
DLA	diffusion-limited aggregation
DP	diffraction pattern
ED	electron diffraction
EELS	electron-energy loss spectrum
IC	integrated circuit
LCD	liquid crystal display
LEED	low energy electron diffraction
ML	monolayer
MOSFET	metal-oxide-semiconductor field effect transistor
OLED	organic light emitting diode
OTFT	organic thin-film transistor
PEEM	photoelectron emission microscopy
PL	photoluminescence
RFID	radio-frequency identification
RT	room temperature
SEM	scanning electron microscopy
STM	scanning-tunneling microscopy
TEM	transmission electron microscopy
TFT	thin film transistor
UPS	ultraviolet photoelectron spectroscopy
XPS	x-ray photoelectron spectroscopy
XRD	x-ray diffraction
ZLP	zero-loss peak

Reproduced with permission of the copyright owner. Further reproduction prohibited without permission.

Chapter 1. Introduction

1.1. Overview of Organic Thin Films

Although the concept of current control based on field effect was proposed as early as the 1930s, silicon-based metal-oxide-semiconductor field effect transistor (MOSFET) was first realized three decades later. Since then, the semiconductor industry has grown into one of the largest industries in the world and become the very foundation for information and communication technologies. Today, the microelectronic industry uses mainly silicon for logic integrated circuits (ICs) and some compound semiconductors, such as GaAs and InP, for optoelectronic devices. Based on complementary metal oxide semiconductor (CMOS) technology, the fabrication process of silicon has been continuously perfected through a huge amount of capital investment in research and development. For decades, silicon CMOS technology has been able to keep up with the demands for smaller and faster logic circuits, following the famous Moore's law. Although there is a theoretical limit on the minimum feature size that can be cost-effectively fabricated on silicon, using the conventional photolithography with ever-decreasing exposure wavelength, it is unlikely that an alternative material can replace silicon for logic ICs in the near future.

Organic nanostructures and thin films represent a departure from the mainstream microelectronics based on inorganic semiconducting materials. In fact, the utilization of organic semiconductors and conductors, such as polyacetylene (the discoverers of which were honored with the Noble Prize in chemistry in 2000), opened a new prospect for microelectronics. The electrical mobility (μ) is one of the most

Reproduced with permission of the copyright owner. Further reproduction prohibited without permission.

important parameters for semiconductors. It describes how fast the charge carriers, electrons or holes, can be transported within the material. This determines the speed at which a logic gate built of this material can be switched on and off, thus the performance of the logic device. In inorganic semiconductors, charge carriers are often described as highly delocalized plane waves in wide energy bands. The carrier mobility is limited only by lattice phonon scattering and decreases with increasing temperature. However, the relatively weak van de Waals inter-molecule interaction in organic semiconductors limits their carrier mobility to approximately 1 to 10 cm^2/Vs. Charge carriers are transported in organic semiconductors by hopping between localized states. The hopping is assisted by phonons. Hence the mobility normally increases with increasing temperature.

The electrical mobility μ of organic semiconductors has been constantly improved in the last decades through discovery of new materials and the perfection of processing techniques for existing materials. The reported values cover a range up to about 0.2 cm^2/Vs for conjugated polymers, reaching the value of hydrogenated amorphous silicon (a-Si:H). For small-molecule organic semiconductors, higher μ values exceeding 1.5 cm^2/Vs are possible (*Jackson, 1998*). But these are still much lower than that of silicon, which has electron mobility in the order of 10^3 cm^2/Vs, depending on its doping level. Therefore, organic thin-film transistors (OTFTs) (*Dimitrakopoulos, 2001*) cannot rival the speed performance of transistors based on single-crystal inorganic semiconductors, such as Si, Ge and GaAs, whose charge-carrier mobility is three or more orders of magnitude higher (*Horowitza, 2004*). Consequently, OTFTs are unlikely to find applications that require high switching

Reproduced with permission of the copyright owner. Further reproduction prohibited without permission.

speed, whereas in applications where large deposition area, good mechanic flexibility and low fabrication cost are important, they can be competitive materials if the manufacturing issues can be solved (*Sheats, 2004; Chabinyc, 2004; Bao, 2000*). The following lists some of the anticipated applications for OTFTs:

- Flexible displays that require large area coverage, mechanical flexibility, or low fabrication cost. These applications include flexible electronic-paper (*Rogers, 2002*), active matrices for flat panel display based on liquid crystal display (LCD) or organic light emitting diode (OLED) technology (*Chen, 2004*), and smart textile or wearable electronics.
- Low cost consumer electronics such as low-end smart cards for access control, radio-frequency identification (RFID) tags and flash memories (*Möller, 2003*).
- Novel sensors (electronic noses) based on the unique responses of organic semiconductors to different chemicals present in the air.

Flat panel displays and RFID tags are the two major high-volume applications anticipated for OTFTs. The competitors here are mainly a-Si:H for display and Si for consumer electronics with ever-shrinking size and cost. One of the main difficulties with a-Si:H is its high deposition temperature, which is incompatible with plastic substrates. However, there is active research into low-temperature a-Si:H deposition which shows great promise.

Currently two categories of organic materials are under investigation within the field of organic electronics (*Kelley, 2004*). On the one hand, there are conjugated polymers, long molecules that can be easily processed, for example, by simple printing

Reproduced with permission of the copyright owner. Further reproduction prohibited without permission.

or spin coating. Oligomers, on the other hand, are small molecules that are generally more difficult to handle, but they allow the preparation of well-ordered films of high purity at or close to room temperature (RT). Although it is hard to predict at this point which category of the organic semiconducting materials will dominate in future organic electronics, so far the devices that have been successfully commercialized are mainly made from oligomers (*Dimitrakopoulos, 2002*). Moreover, the recent demonstration of efficient electroluminescence from organic thin film devices based on oligomers promises to transform the flat-panel display industry (*Tang, 1987; Burrows 1994; Burroughes, 1990*), with the potential of replacing LCDs with an entirely new generation of efficient, emissive, full-color flat panels based on OLEDs. In more recent developments, organic thin films are showing promise for use as thin film transistors (TFTs) (*Dodabalapur, 1995; Garnier, 1997*) and might eventually replace amorphous or polysilicon TFTs currently used in the back plane of active matrix liquid crystal display (AMLCD). These new developments must also be placed in the context of continued efforts and progresses that have been directed at employing organic thin films for solar-energy conversion (*Hoppe, 2004; Coakley, 2004*) and in sensors of various kinds.

1.2. Pentacene Crystals

The most widely studied organic semiconductor is pentacene (*Ruiz, 2004*). As shown in Figure 1.1, pentacene ($C_{22}H_{14}$) is a planar molecule with five benzene rings fused in a straight line. Pentacene stands out among many organic semiconductors for its relatively high field-effect mobility and its ability to form ordered films on various types of substrates, making it one of the best candidates for OTFTs. Figure 1.2 shows

Reproduced with permission of the copyright owner. Further reproduction prohibited without permission.

the mobility of the most common p-type organic semiconductors versus their time of development. Pentacene has the highest electrical mobility ever reported for organic semiconductors. High mobility, above 1 cm^2/Vs, can be routinely achieved with pentacene using optimized processing. Actually, a field effect mobility of 5 cm^2/Vs was obtained with an OTFT made from pentacene with polymer surface pre-treatment as early as 2 decades ago (*Turner-Jones, 1987*).

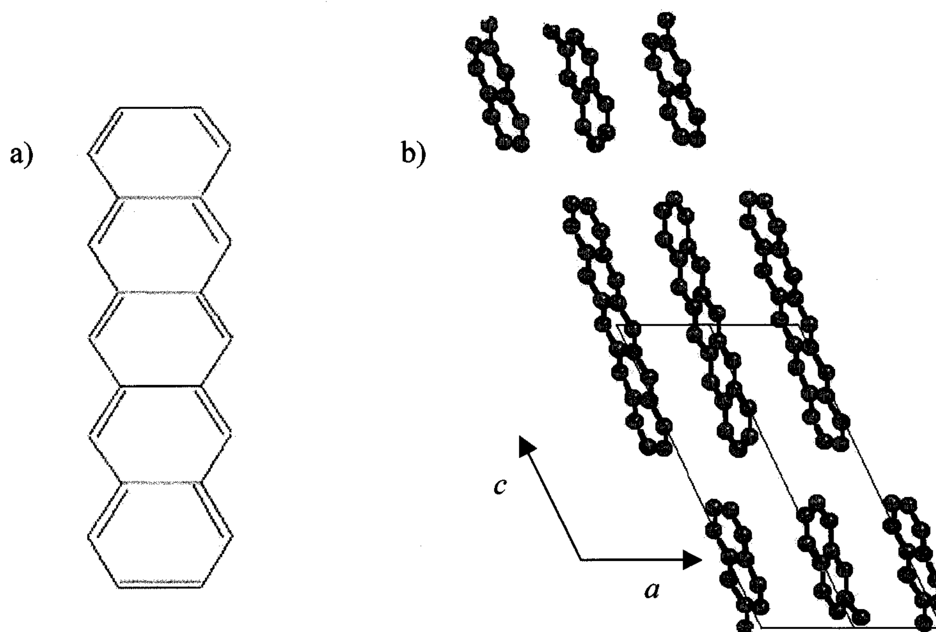

Figure 1.1. (a) Pentacene molecular structure and (b) bulk crystalline structure of pentacene with lattice parameters: $a=7.93\pm0.02$ Å, $b=6.14\pm0.02$ Å, $c=16.03\pm0.05$ Å, $\alpha=101.9°$, $\beta=112.6°$, $\gamma=85.8°$, viewed along the [010] axis.

Different deposition methods can be used for pentacene thin films, including solution based dipping and spin coating, as well as vapor phase high-vacuum evaporation. Since the charge transport properties in deposited pentacene (and other semiconducting oligomers as well) depend on an efficient π-orbital overlap between neighboring molecules in the film, it is important to understand the structure and

Reproduced with permission of the copyright owner. Further reproduction prohibited without permission.

molecular packing of pentacene thin films, as well as the growth mechanisms that produce such structures. This basic understanding of film growth mechanisms will benefit the optimization of material properties through process perfection.

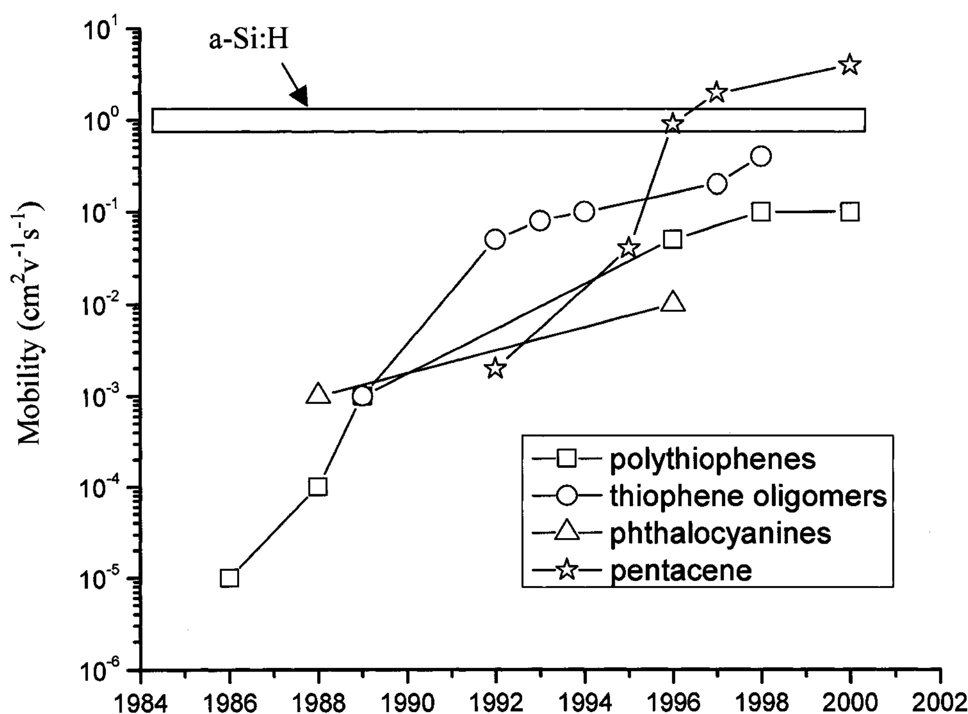

Figure 1.2. Mobility of p-type organic semiconductors versus time of development. (Dimitrakopoulos, 2002).

Pentacene crystallizes in a layered structure and has a triclinic unit cell, space group $P\bar{1}$. There are two molecules per unit cell, positioned at (0,0,0) and $(\frac{1}{2},\frac{1}{2},0)$ and arranged in a herringbone configuration, as shown in Figure 1.1(b). The interplanar spacing $d(001)$ is commonly used to identify the polymorphs of pentacene thin films. Pentacene exhibits structural polymorphism with two known polymorphs having the $d(001)$ spacing of 14.1 Å (*Campbell, 1961*) and 14.4 Å (*Holmes, 1999*)

Reproduced with permission of the copyright owner. Further reproduction prohibited without permission.

found in the bulk single-crystal phase. However, it has been reported that the crystal structure of thin-film pentacene is different from the bulk single crystal (*Dimitrakopoulos, 1996*). There are also polymorphs existing in thin films, having *d*(001) spacing of 15.0 Å and 15.4 Å, depending on the method and deposition conditions used. The "thin film" and "bulk phase" phases can coexist in a pentacene thin film when a certain critical thickness is exceeded, either deposited at room temperature or at elevated temperature.

1.3. Characterization of Pentacene Thin Films

In principle, it is desirable to apply a whole battery of experimental methods that have been developed to characterize the structures and properties of deposited thin films to pentacene. Scanning electron microscopy (SEM) (*Dimitrakopoulos, 1996*), photoelectron emission microscopy (PEEM) (*Heringdorf, 2001*) and AFM are employed to obtain direct (real space) images to study morphology of thin films. Unfortunately organic thin films are generally sensitive to the electron beam and provide poor image contrast in electron microscopy. Therefore, AFM is probably the most widely applied method for characterization of post-deposited films. It can be an excellent tool for detecting ultra-thin films and small-scale surface features. Scanning-tunneling microscopy (STM) has been employed to identify the orientation of pentacene molecules deposited on semiconducting and metallic crystals.

Monitoring the diffraction pattern by XRD, electron diffraction (ED) or low energy electron diffraction (LEED) during or after the thin-film growth can yield information on crystallographic orientation, the degree of order or domain arrangement within a polycrystalline film. Among these methods, XRD is particularly

Reproduced with permission of the copyright owner. Further reproduction prohibited without permission.

powerful as it can monitor both first-layer formation and thicker films in real time, as well as extracting information on the crystalline quality of the films. Electron diffraction opens the possibility to study the films and their orientation at high spatial resolution (limited by radiation damage).

Beyond probing crystalline structure, the electronic structure is another important parameter relevant to thin film properties. X-ray and ultraviolet photoelectron spectroscopy (XPS and UPS) are used to measure the density of filled electron states, relative to the vacuum level. Optical techniques applied to pentacene thin films include UV-Vis spectroscopy and IR spectroscopy to measure the absorption properties and photoluminescence measurements to assign the electronic structure.

1.4. Outline of This Thesis

The outline of the thesis is described below. In Chapter 2, the morphology and structure of vacuum-evaporated pentacene thin films are studied as a function of substrate temperature and evaporation rate. From AFM images it will be shown that lateral dimensions of individual crystallite can be several tens of microns in polycrystalline films. Furthermore, the morphology and structure of ultra-thin films was studied, to better understand the growth mode during initial stages of pentacene film formation. A transition in the growth mode, from 2D to 3D at a film thickness of about 1.6 nm was observed.

The electron-beam sensitivity of pentacene films was investigated in Chapter 3. The decay of a diffraction pattern and decay of electron-energy loss features was

Reproduced with permission of the copyright owner. Further reproduction prohibited without permission.

monitored to study electron beam radiation damage. In Chapter 4, optical properties of pentacene thin films, such as absorption and photoluminescence, as well as the optical properties calculated from electron-energy loss spectrum (EELS), are discussed. Finally, Chapter 5 summarizes the results presented in the thesis and discusses directions for possible future work.

Reproduced with permission of the copyright owner. Further reproduction prohibited without permission.

Chapter 2. Morphology, Structure and Growth of Pentacene Thin Films

2.1. Introduction

The charge carrier mobility of organic thin films is one of the most important parameters as far as semiconducting properties are concerned. It has a striking dependence on the morphology, such as grain size and grain boundaries, and structure of thin films *(Karl, 2003)*. Moreover, it was found that the carrier mobility of organic thin films is independent on thickness. It is believed that the charge carrier transport is dominated by the first few monolayers of a thin film (*Dodabalapur, 1995*). Therefore, it is crucial to study the morphology and structure of pentacene thin films, particularly film formation during the early stage of growth.

Organic thin films can be deposited by sublimation in a variety of vacuum-deposition systems and highly ordered thin films of pentacene can be obtained at low substrate temperature, such as room temperature. However, the basic physical principles governing organic thin-film growth and crystallization are not yet well understood. Thus, many research groups are studying the growth of organic thin films. It was found that, in some cases, organic thin-film growth closely mimics epitaxial growth of inorganic materials (*Heringdorf, 2001*). Therefore, concepts from film growth of inorganic materials have been used to interpret the growth of organic thin films on inert substrates (*Verlaak, 2003*). However, there are both similarities and fundamental differences between inorganic and organic materials.

Reproduced with permission of the copyright owner. Further reproduction prohibited without permission.

Generally, thin film formation involves one of the three basic growth modes: layer-by-layer (or Frank-Van der Merwe mode), island mode (or Volmer-Weber mode) and layer-plus-island (or Stranski-Krastanov mode). In the inorganic case, island growth mode occurs when the interactions among the adsorbed atoms are stronger than the interactions between adsorbed atoms and the substrate. The layer growth mode occurs when the adatoms diffuse to form two-dimensional islands and are more strongly bonded to the substrate than to other atoms. The layer-plus-island mode is an intermediate combination of the aforementioned modes. In this case, after forming one or more layers, forming a subsequent layer becomes less favorable and islands form. However, in an organic material, such as pentacene, the interactions between molecules within the crystal are the rather weak van der Waals interactions. Moreover, the molecule-molecule and molecule-substrate interactions have a pronounced anisotropy related to the shape of the molecules (*Forrest, 1997*). Thus, the conditions for growth of high quality films will depend on a delicate balance between the intra-molecular forces, inter-molecular forces and molecule-substrate interaction. In any case, the atom- or molecule-substrate interaction is an important parameter controlling the growth mode.

In this chapter, we discuss the formation of pentacene thin films, deposited by thermal evaporation in a high vacuum system, on different substrates. A transition from 2D mode to 3D mode was observed in the early stages of film growth. The size of individual crystallites within the polycrystalline films varied as a function of substrate temperature and evaporation rate. The growth conditions that affect the quality of the films were investigated, as well as the effects of annealing of the

Reproduced with permission of the copyright owner. Further reproduction prohibited without permission.

pentacene films after deposition. The structure of thin films was determined by XRD and ED. The assignment of Miller indices to the diffracting planes in both XRD and ED allowed us to determine the crystallographic orientation of the studied films.

2.2. High Vacuum Evaporation Setup

Pentacene powder, with a purity of 98%, was purchased from Sigma-Aldrich. No further purification was applied prior to any of the experiments discussed below. Pentacene thin films were obtained by thermal evaporation in a high vacuum environment with a base pressure of 2×10^{-6} Torr. The deposition system is schematically shown in Figure 2.1. The source material was loaded in a quartz tube, which was used as a Knudsen evaporation cell. The tube diameter was 5 mm and it was surrounded by a resistively-heated molybdenum wire spiral connected to a transformer. The source material was evaporated at source (Knudsen cell) temperatures between 240 °C and 260 °C, controlled by changing the heater current. The temperature of the substrate holder could be changed (increased) by a halogen bulb (12 V, 75 W), heating from the back of the substrate holder.

The temperature of the source material and the substrate were monitored by K-type fine-wire thermocouples. The evaporation rate was monitored by an in-situ quartz-crystal thickness monitor. A shutter was closed in front of the substrate while adjusting the evaporation rate to a desired constant value. Then substrates were exposed to a constant evaporation flux for a desired time period. In some experiments a shadow mask, separated from the substrate by a distance of 2 mm, was employed to cover part of the substrate.

Reproduced with permission of the copyright owner. Further reproduction prohibited without permission.

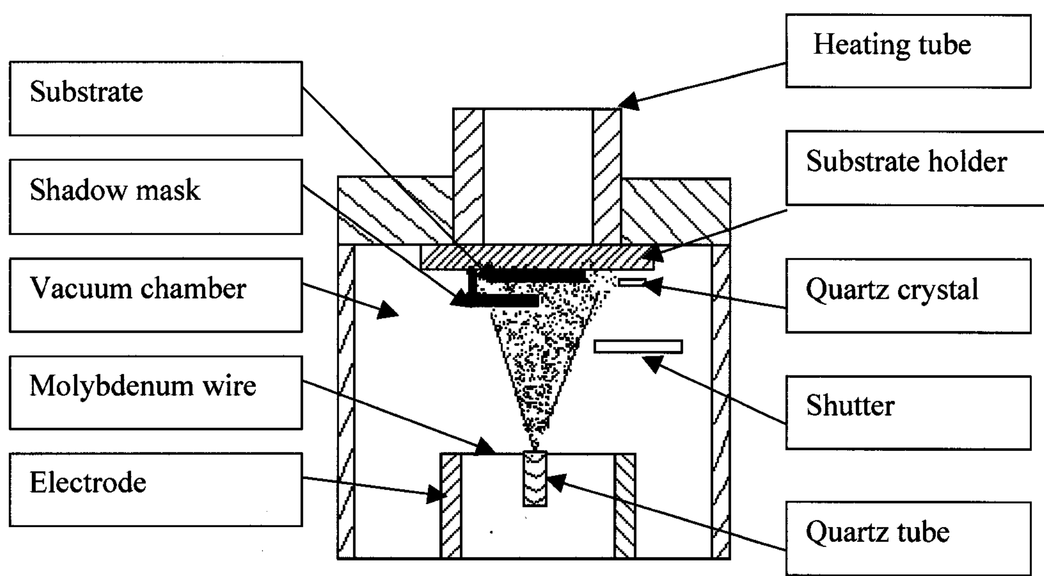

Figure 2.1. Thermal evaporation setup for pentacene thin film deposition.

2.3. Crystallographic Orientation of Pentacene Thin Films

To investigate the crystallinity of the deposited films, XRD measurements were performed with monochromatic Cu $K\alpha$ (λ =1.54 Å) radiation and ED measurements were done in TEM. For XRD measurements, pentacene thin films were deposited onto two types of substrates. One is bare Si(001), which was cleaned in piranha etch (H_2SO_4:H_2O_2 = 3:1) and then dipped in HF (1 minute) and dried. On the Si substrate the pentacene films were deposited at a rate of 0.1 Å/s at RT, up to a thickness of 100 nm. The other type of substrate is Si(001) wafers coated (by electron-beam evaporation) with amorphous carbon. On this substrate, pentacene thin films were deposited at an evaporation rate of 0.5 Å/s to a thickness of 70 nm at substrate temperatures of 20 °C, 40 °C and 60 °C, respectively. The carbon coated Si substrates were used to allow a direct comparison of film deposited onto carbon-coated grids studied in TEM to films studied by XRD. For ED measurement, pentacene was

Reproduced with permission of the copyright owner. Further reproduction prohibited without permission.

deposited at 20 °C onto amorphous-carbon covered TEM grids at a deposition rate of 0.5 Å/s, up to a thickness of 70 nm.

2.3.1. Ratio Method to Index Diffraction Patterns

We calculated the interplanar spacings, called *d* spacings, of each set of planes (*hkl*) using the crystallographic formula appropriate for a triclinic system (*Hunter, 1984*), as shown in Table 2.1. The ratio of *d* spacing for each plane with respect to (100) or (010) plane was calculated. The experimentally obtained ratios of *d* spacing of each unknown plane (with respect to the plane having the largest *d* spacing) were compared with the theoretically calculated ratios. Then the Miller index of each plane was assigned for planes with corresponding ratios.

Table 2.1: d-spacings and corresponding reflection planes assigned for the inner 10 rings in diffraction pattern of pentacene thin films deposited at RT.

Ring No.	**1**	**2**	**3**	**4**	**5**	**6**	**7**	**8**	**9**	**10**
***d*-spacing [Å]**	6.05 ±0.12	4.71 ±0.07	3.80 ±0.04	3.22 ±0.03	3.01 ±0.02	2.90 ±0.02	2.41 ±0.01	2.34 ±0.01	1.95 ±0.01	1.83 ±0.01
Miller indices (*hkl*)	(010)	(110)	(200)	(210)	(020)	(120)	(220)	(310)	(130)	(320)

We took the lattice parameters of pentacene based on the bulk structure reported by Campbell et al. (*Campbell, 1961)*: a = 7.93±0.02 Å, b = 6.14±0.02 Å, c = 16.03±0.05 Å; α = 101.9°, β =112.6°, γ = 85.8°; and also its "thin film phase" structure: a = 6.1 Å, b = 7.6 Å, c = 15.3 Å; α = 81.0°, β = 85.0°, γ = 89.5° (*Wu, 2004*) for

Reproduced with permission of the copyright owner. Further reproduction prohibited without permission.

calculations of d spacings. Using these values we obtained good agreement between the calculated and experimental values of d-spacing ratios (see Appendix).

2.3.2. Calibration of the Camera Constant in a TEM

As depicted in Figure 2.2, a diffraction spot is located on the photographic film at a distance R from the center of the diffraction pattern. The effective distance between the specimen and the film is designated as the camera length L, and by simple geometry $\tan(2\theta) = R/L$. According to the Bragg Law $\lambda = 2d\sin\theta$, since the diffraction angle θ of the electrons is very small (less than 5 mrad), the approximation $\tan(2\theta) = 2\sin\theta$ is valid, and thus gives $Rd = \lambda L$. Values of R, L and λ for a particular diffraction spot or ring can be measured. Providing that the value of L was calibrated, the d spacing of the set of lattice planes giving rise to that ring can be determined.

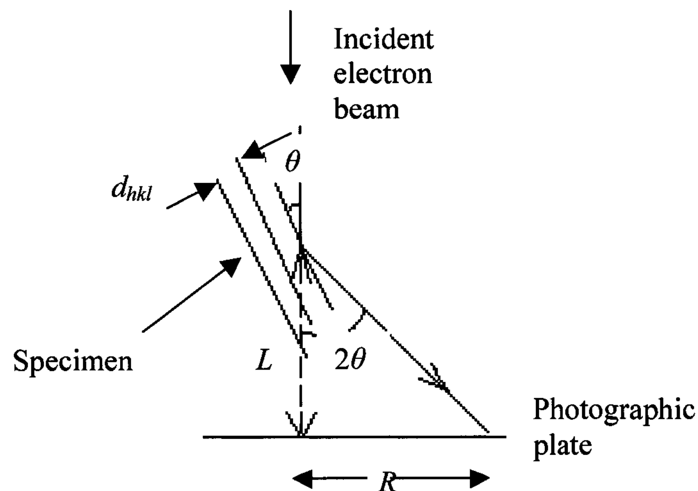

Figure 2.2. Schematic diagram of a simple electron diffraction camera.

Reproduced with permission of the copyright owner. Further reproduction prohibited without permission.

We used a NiO film (that has NaCl cubic crystal structure) as a standard for camera length calibration. NiO calibration sample is a fine-grained polycrystal and gives a diffraction pattern consisting of sharp rings. The diameter D_{hkl} of each ring was measured instead of its radius, because a shutter was used to avoid damage of the CCD detector by strong beam and it blocked the center of diffraction pattern (DP) rings. Then the measured D_{hkl} plotted against known d_{hkl} of the calibration sample gives a straight line, whose slope provides a value of camera length constant ($2\lambda L$). After calibrating the camera constant, we recorded diffraction patterns of the pentacene samples at the same nominal camera length and same objective lens excitation. Then the diameters of each ring were measured, and corresponding d spacing can be calculated using $d_{hkl} D_{hkl} = 2\lambda L$.

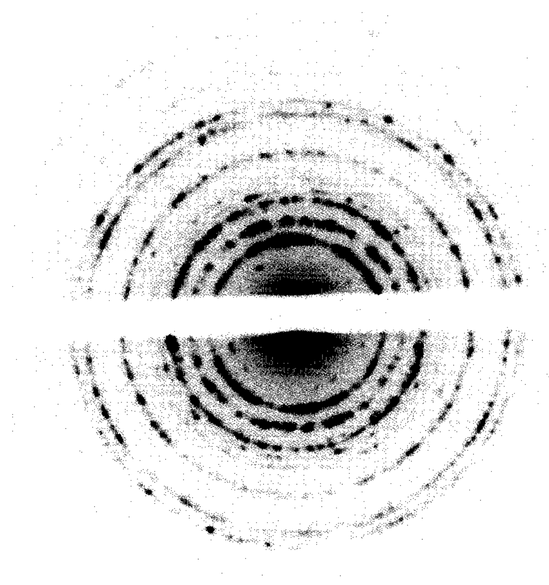

Figure 2.3. DP of pentacene thin films deposited on amorphous carbon film at RT with a thickness of 70 nm.

Reproduced with permission of the copyright owner. Further reproduction prohibited without permission.

The DP of pentacene thin films deposited on amorphous carbon film at RT shows polycrystalline characteristics, as shown in Figure 2.3. The *d* spacings for the inner 10 rings were calculated, and the corresponding reflection planes were assigned by comparing the ratios with theoretical ratios listed in Table 2.1.

To further establish the assignment of Miller index for each reflection plane, we simulated the crystal structure viewed in the reciprocal space along [001] direction (see Figure 2.4) using the CrystalKit software (*www.totalresolution.com*). The ring indices assigned from our experimental match with the theoretical results.

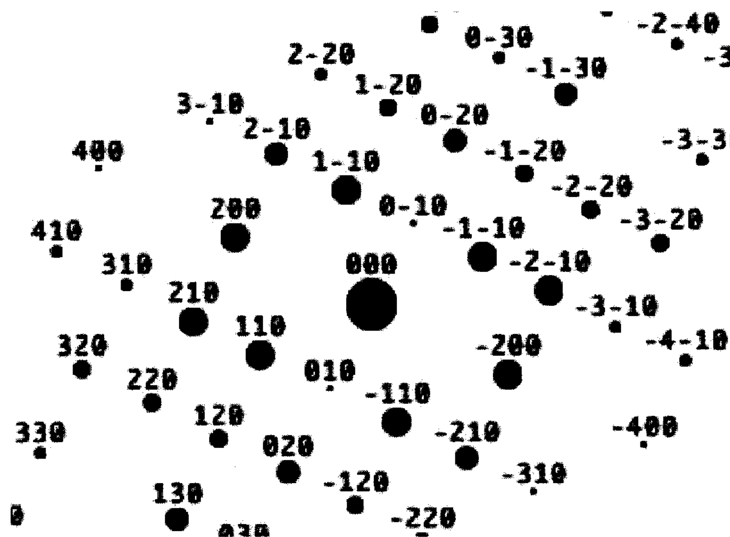

Figure 2.4. Indexed reciprocal lattice points for a pentacene single crystal, with incident electron beam along [001] direction.

Shown in Figure 2.5 is the XRD spectrum of pentacene deposited on amorphous carbon film at RT. The peak positions and corresponding *d* spacings, ratios

Reproduced with permission of the copyright owner. Further reproduction prohibited without permission.

and designated (*hkl*) are listed in Table 2.2. The films deposited on amorphous carbon at substrate temperatures of 40 °C and 60 °C were also analyzed by XRD. The films were deposited on carbon-coated Si(001) as described above. The films show the presence of two phases at elevated deposition temperatures with *d*(001) of 15.24 Å and *d*(001) of 14.33 Å, respectively. This will be explained in section 2.5. We also measured films deposited on clean Si(001) (as described above) at RT by XRD. This is (i.e. the XRD of the film on Si) shown in Figure 2.6, and the *d*(001) spacing is also 15.3 Å. The results of *hkl* assignment for the films on clean Si are the same as for films deposited on carbon.

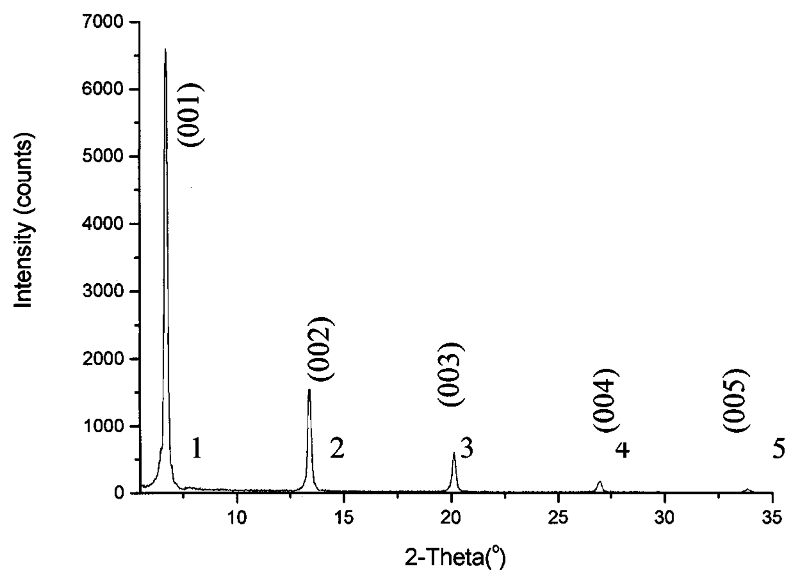

Figure 2.5. XRD spectra of pentacene deposited on amorphous carbon film at RT with a thickness of 70 nm.

Reproduced with permission of the copyright owner. Further reproduction prohibited without permission.

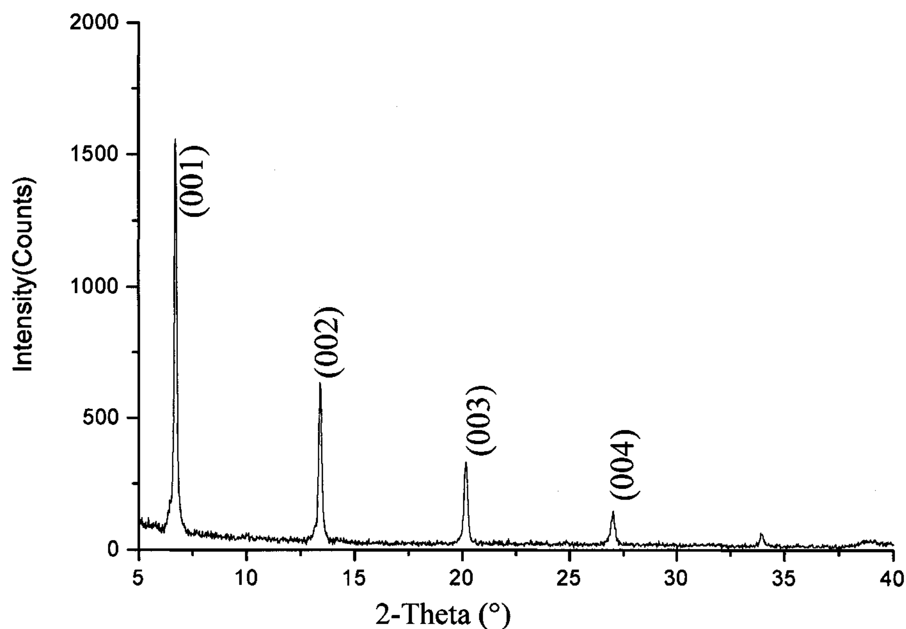

Figure 2.6. XRD spectra of pentacene deposited on Si (001) at a rate of 0.1 Å/s at RT with a thickness of 100 nm.

Table 2.2: Measured data from XRD of pentacene thin film deposited on C film.

Peak	2-Theta [degree]	Measured *d* [Å]	Ratio	(*h k l*)
1	6.7	15.29	1	001
2	13.4	7.67	0.50	002
3	20.1	5.12	0.33	003
4	26.9	3.84	0.25	004
5	33.8	3.07	0.20	005

In ED experiments, only planes of type (*hk*0) were seen. This indicates that the incident electron beam is perpendicular to substrate and the (001) planes are parallel to the substrate in our films. In XRD experiments, only (00*l*) planes in the films can be

Reproduced with permission of the copyright owner. Further reproduction prohibited without permission.

seen. Therefore, in pentacene thin films deposited at RT or elevated temperatures (40 °C and 60 °C), the *ab* plane (00*l*) is oriented parallel to the substrate. And the *c* axis of the triclinic crystal is almost perpendicular to the substrate.

2.3.3. Textured Polycrystalline Structure

For many polycrystalline specimens, the distribution of crystal orientation is not random; instead, one lattice plane may lie preferentially parallel to the specimen plane. In this plane, the crystals are rotated randomly around a common axis, the fibre axis of fibre texture (*Pinsker, 1953*). In our pentacene films, the *ab* planes (00*l*) within pentacene films are parallel to the substrate, as described above. Therefore, textured polycrystalline structure should exist. The existence of the fibre axis means that the reciprocal-lattice points are distributed around concentric circles centered on the fibre axis. A fibre texture can be recognized clearly if the direction of electron incidence is titled through an angle β relative to the fiber axis. In practice, the specimen normal is titled relative to the electron beam in an object goniometer. Then the intersections of the Ewald sphere with the concentric circles become sickle-shaped or arc shaped.

Figure 2.7 shows the diffraction patterns at different position as a function of tilting angle β, which is the angle between the specimen normal and electron beam. When β = 15°, there is not much difference in DP, comparing to β = 0°. The diffraction patterns present ellipse when β = 30°. Due to limitation of tilting in TEM, diffraction patterns can't be observed at larger tilting angles, and no quantitative results from this measurement can be obtained. However, we can qualitatively confirm that the *ab* planes within pentacene films do parallel to the substrate and the fibre axis is parallel to the *c* axis, which is common in layered structure.

Reproduced with permission of the copyright owner. Further reproduction prohibited without permission.

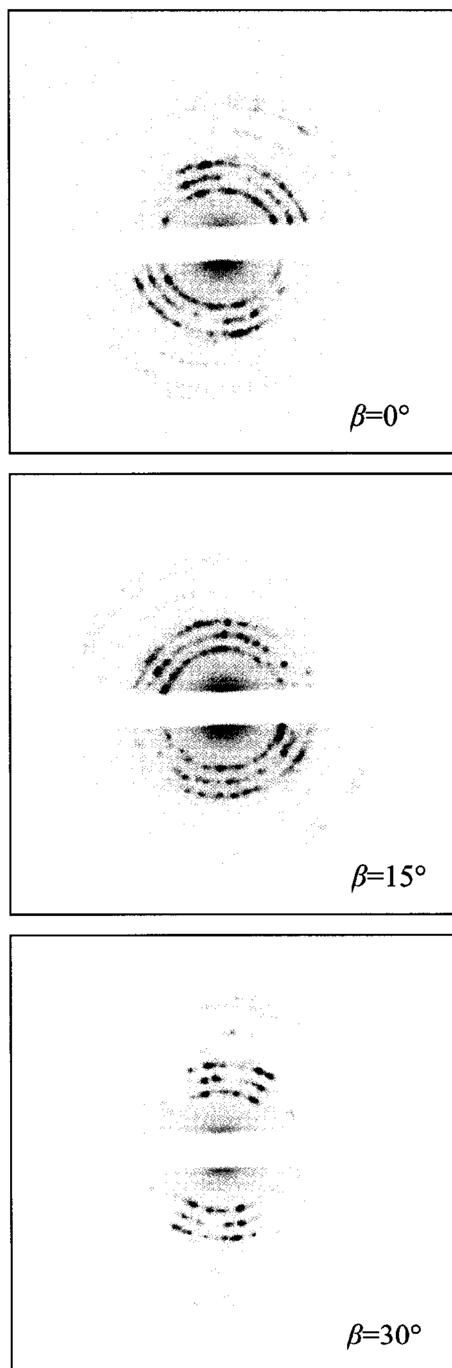

Figure 2.7. Diffraction patterns of pentacene films taken at a tilting angle β is 0°, 15° and 30°, respectively.

Reproduced with permission of the copyright owner. Further reproduction prohibited without permission.

2.4. Evolution of Pentacene Thin Film Growth

2.4.1. Experiment Details

In order to study the morphology and structure evolution of pentacene with increasing film thickness, we used a shadow mask. This results in a region of sample films with a thickness gradient from zero to about 70 nm. The shadow mask was separated 2 mm from the substrate as shown in Figure 2.1. The substrate was 10 nm carbon stretched on TEM grids and deposited on glass slides. The deposition rate was 1 Å/s and the deposition time is up to 20 minutes. Different thickness could be observed under the mask edge. This is because the shadow mask results in a reducing deposition rate as one moves towards the masked area of the sample. This is equivalent to same deposition time but different pentacene growth rate.

To test whether the morphology and structure observations are results of decreased deposition rate or they are genuine film-thickness effect, we grew pentacene thin films with varying thickness at the same evaporation rate of 0.1 Å/s. All depositions were done at room temperature. The substrates for this experiment were TEM grids coated with carbon film and the glass holder was ultrasonically cleaned in methanol.

Characterization was done using a JEOL 2010 TEM operated at 200 keV with an electron beam current density between 0.1 A/cm^2 and 1.34×10^{-3} A/cm^2. To prevent electron radiation damage, the total dose used is less than the characteristic dose of 0.1 C/cm^2, which will be discussed in Chapter 3. In order to avoid electron-beam damage, electron beam was also blocked, which is controlled by a script written for the

Reproduced with permission of the copyright owner. Further reproduction prohibited without permission.

microscope console, and a fresh area was moved into the beam before recording each image. The topography of pentacene films was characterized by tapping mode of Digital Instruments AFM. When in the tapping mode, the cantilever is oscillated at its resonant frequency and positioned above the surface, so that it only taps the surface for a very small fraction of its oscillation period. During this short time, the lateral forces are dramatically reduced as the tip scans over the surface. Therefore, in tapping mode low contact forces were used, resulting in less damage to samples. We used silicon cantilever (NSC15) for this experiment. Its resonant frequency is approximately 325 kHz. The radius of curvature is less than 10 nm and the reflective side is coated with Al.

2.4.2. Results and Discussions

We observed the entire evolution of the nucleation and growth steps to form a continuous film in our experiments. In the following paragraphs, we describe this evolution of pentacene film growth as four stages (*Maissel, 1983*): island stage, coalescence stage, channel stage and development of a continuous film.

1) The Island Stage

The growth of thin films is controlled by kinetic processes such as diffusion and aggregation and may be understood within an established theoretical framework (*J. A. Venables, 1994; Amarl, 1994*). During the initial stage of growth, molecules diffuse until they randomly combine to nucleate a stable island. Further nucleation occurs until the characteristic separation of nucleated islands is comparable with the diffusion length of adsorbed molecules. Nucleation of new islands is suppressed at this point

Reproduced with permission of the copyright owner. Further reproduction prohibited without permission.

and lateral growth of existing islands proceeds through the capture of diffusing molecules and continues until neighboring islands meet. In our case we observed the similar behavior. The stable two-dimensional (2D) islands nucleate on the surface. We define a 2D island as a single molecular layer of crystalline pentacene with a thickness of approximately 16 Å, corresponding to pentacene molecules oriented with their long molecular axis perpendicular to the substrate. Two different shapes of pentacene islands were observed during this stage. One is dendritic, as shown in Figure 2.8(a) and Figure 2.8(b); the other is a smooth-edge shape, as shown in Figure 2.8(c), Figure 2.9(a) and Figure 2.10(a). It is known that the classical nucleation density N is determined by the ratio F/D_s, where F is the growth rate and D_s is the diffusion constant of pentacene on the substrate. The nature of substrate and the temperature both affect the diffusion constant D_s. For the same substrate and at the same deposition temperature, supposing the diffusion constants are the same, then the nucleation density is determined by the growth rate only. With sufficiently low nucleation density, a fractal island shape can always be observed. Fractal growth will occur when the molecular hopping time on the surface is much smaller than the hopping time on a step-edge and the fractal dimension exhibits classical diffusion-limited aggregation (DLA). When the fractal dimension constant is equal to 2, the islands are smooth-edge shape (*Heringdorf, 2001*).

2) The Coalescence Stage

Two islands can touch, as shown in Figure 2.10(b), and coalesce to form a new island occupying an area smaller than the sum of the original two, thus exposing bare substrate surface. As shown in Figure 2.8(d), 2.10(c) and 2.11(b), this process is

Reproduced with permission of the copyright owner. Further reproduction prohibited without permission.

characterized by a decrease in total projected area of the nuclei on the substrate (~50% of the substrate is bare after coalescence as opposed to 20% substrate bare just prior to this stage). The height of an island increases during the coalescence step, as shown in AFM images in Figure 2.9. The shape of islands changed from regular rounded to fringed or triangular profile.

The driving force for this behavior is the reduction in surface energy. If the surface energy were independent of the crystal orientation, it would act to reduce the surface area to a minimum by producing spherical nuclei (*Maissel, 1983)*. This would, however, require significant amount of diffusion to rearrange the deposited material. To find out whether the crystal orientation changes during this step, we recorded the diffraction patterns before and after the shape change, as shown in Figure 2.12. The *d* spacings of the inner three visible rings are 0.47, 0.39 and 0.32 nm, respectively, which are the same as those of the thicker films (discussed in Section 2.3). This suggests that there was no change of crystal orientation during the coalescence stage.

3) The Channel Stage

After coalescence of the first monolayer as described above, 3D islands (with height more than one ML) grow further as deposition is continued as shown in Figure 2.8(e). A competition between growth due to diffusive capture and the incorporation of molecules directly incident in the islands arises. Secondary nucleation occurs around an island edge and also on top of an island, as witnessed by Figure 2.8(e). Thus the layer- plus-island growth mode (3D) was observed. The islands became elongated and joined to form a continuous network structure, as shown in Figures 2.8(f), 2.10(d)

Reproduced with permission of the copyright owner. Further reproduction prohibited without permission.

and 2.11(c). Eventually, the film becomes continuous but contains many irregular holes.

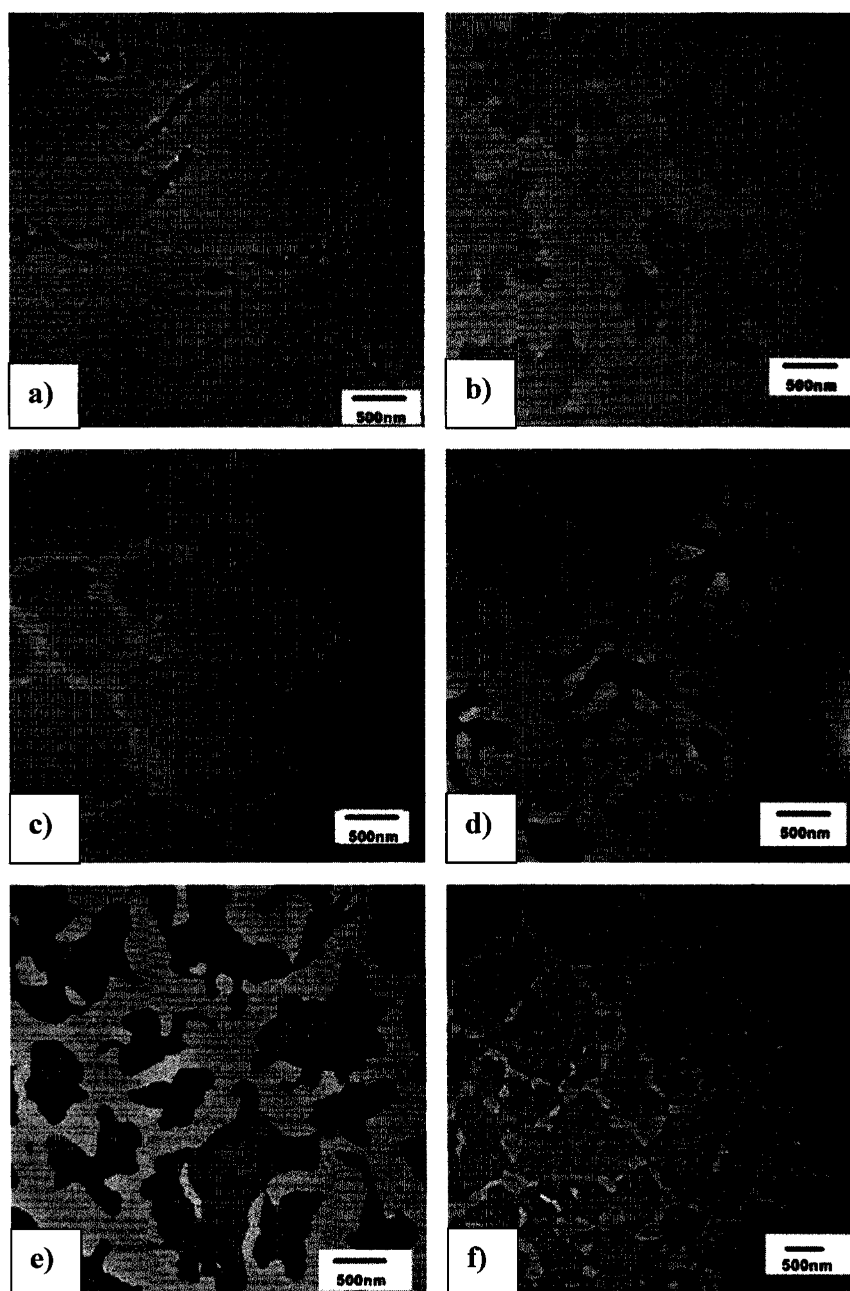

Figure 2.8. TEM images of pentacene ultra thin film formation with gradient thickness from a) to f), obtained by using shadow mask.

Reproduced with permission of the copyright owner. Further reproduction prohibited without permission.

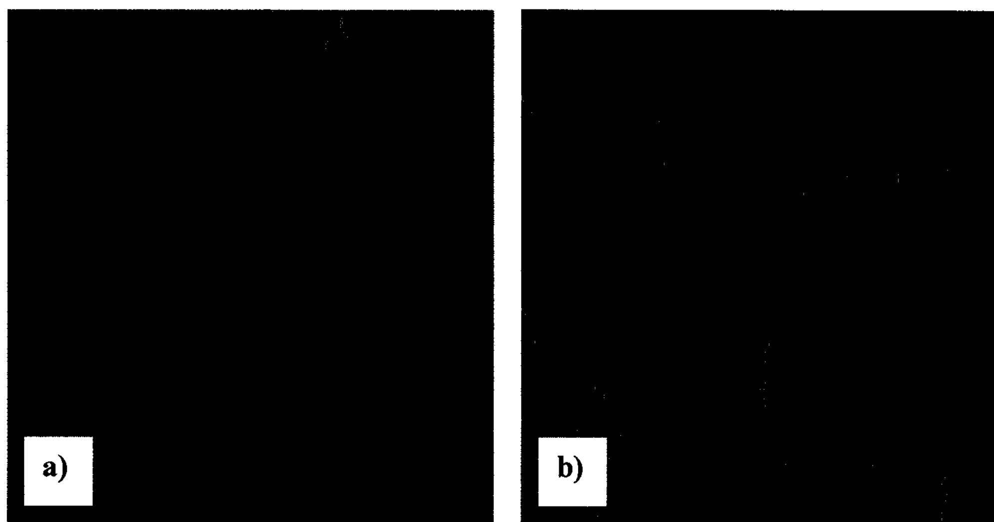

Figure 2.9. AFM images (5 μm × 5 μm) of pentacene deposited onto carbon films using shadow mask.

4) Continuous Film

Figure 2.13(a) shows that a pentacene film deposited onto glass is a continuous network of pentacene with obvious holes, with the height of the individual islands reaching approximately 10 nm. From AFM profile of one island, as shown with a circular sign in the AFM image in Figure 2.13(a), terrace are obvious and the height of each layer in the image is about 1.6 nm, corresponding to one layer of pentacene molecules with their c-axis aligned perpendicular to the substrate. Therefore, it appears that after the 2D growth of the first monolayer (including coalescence and shape changes), the growth mode changes to a 3D mode. As deposition continues to a thickness beyond 70 nm, as shown by AFM image in Figure 2.14, pentacene islands connect together to form continuous and larger grains with lamellar shape

Reproduced with permission of the copyright owner. Further reproduction prohibited without permission.

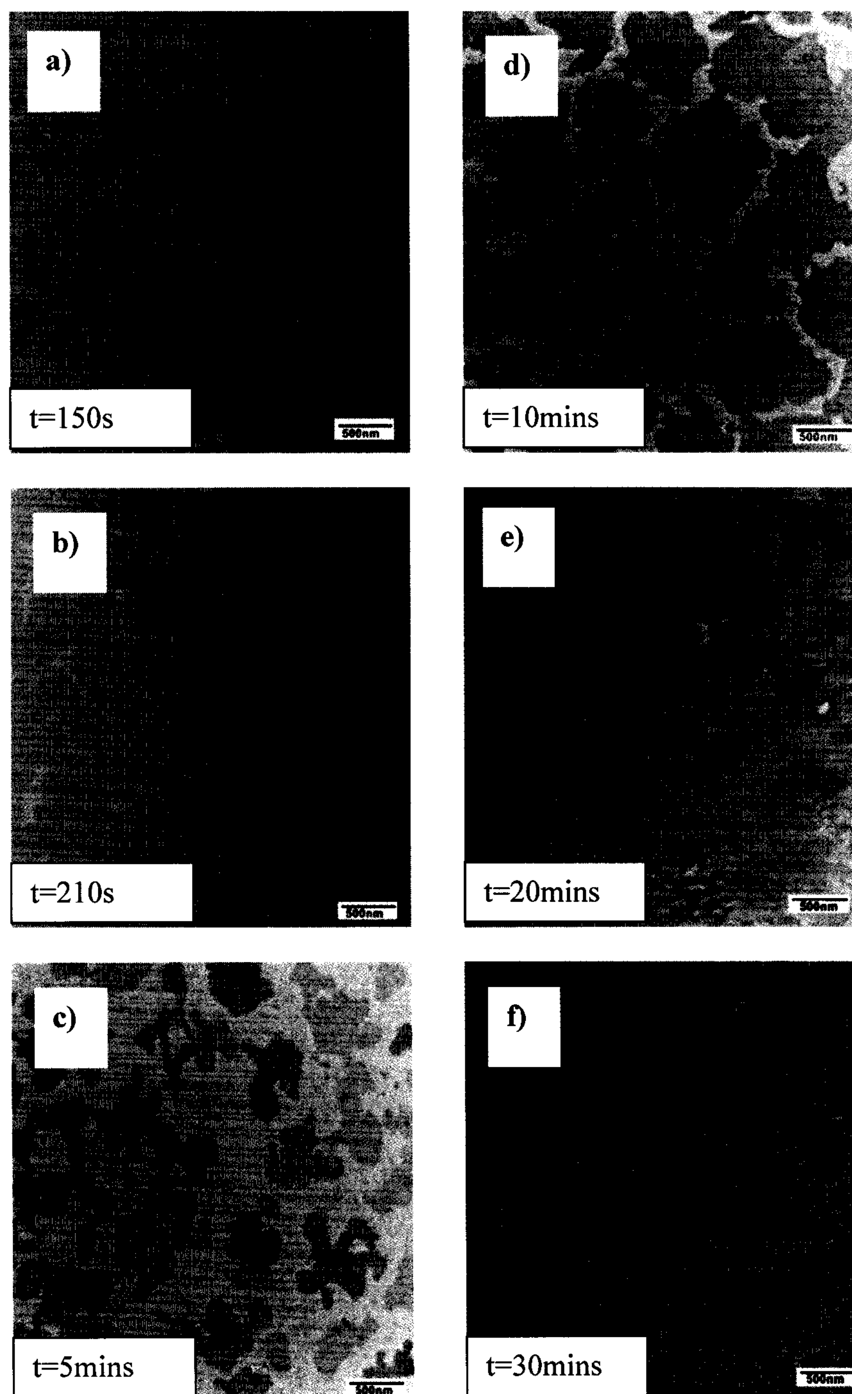

Figure 2.10. TEM images of pentacene thin films formation with gradient thickness from a) to f), obtaining by varing the deposition time, with the same evaporation rate 0.1 Å/s at RT onto carbon pre-covered TEM grids.

Reproduced with permission of the copyright owner. Further reproduction prohibited without permission.

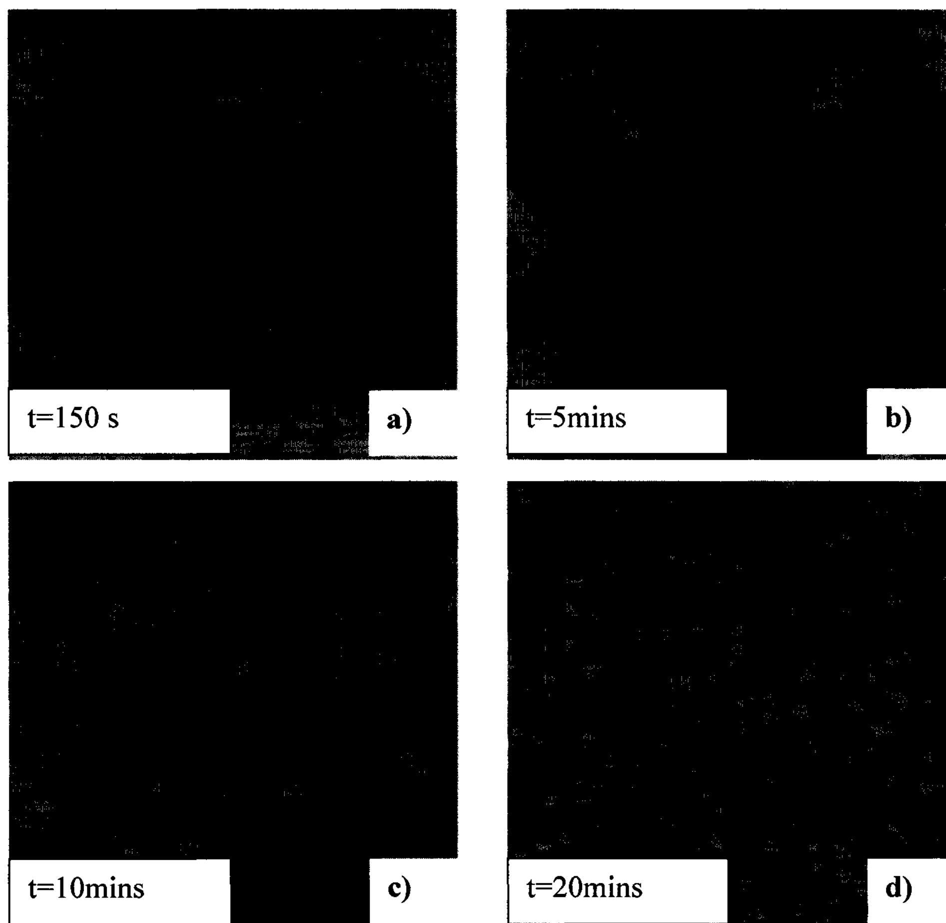

Figure 2.11. AFM images of pentacene thin film formation with thickness gradient from a) to d), obtaining by varing the deposition time, with the same evapration rate 0.1 Å/s at RT onto glass. The size of image is 5 μm × 5 μm.

Reproduced with permission of the copyright owner. Further reproduction prohibited without permission.

Figure 2.12. Diffraction patterns of the pentacene islands. Left: before shape change; right: after shape change.

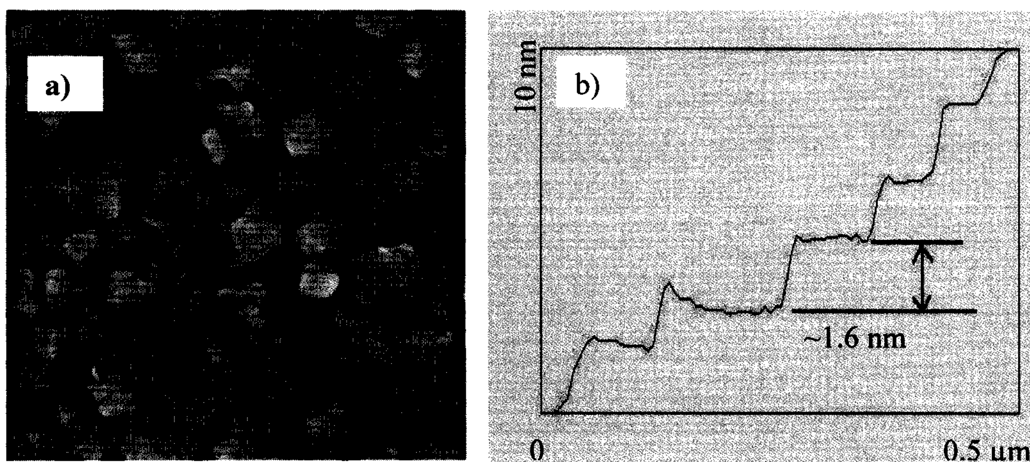

Figure 2.13. a) AFM image (2 μm × 2 μm) of pentacene films deposited onto glass at a rate of 0.1 Å/s at RT; b) profile of one island with height of about 10 nm.

Reproduced with permission of the copyright owner. Further reproduction prohibited without permission.

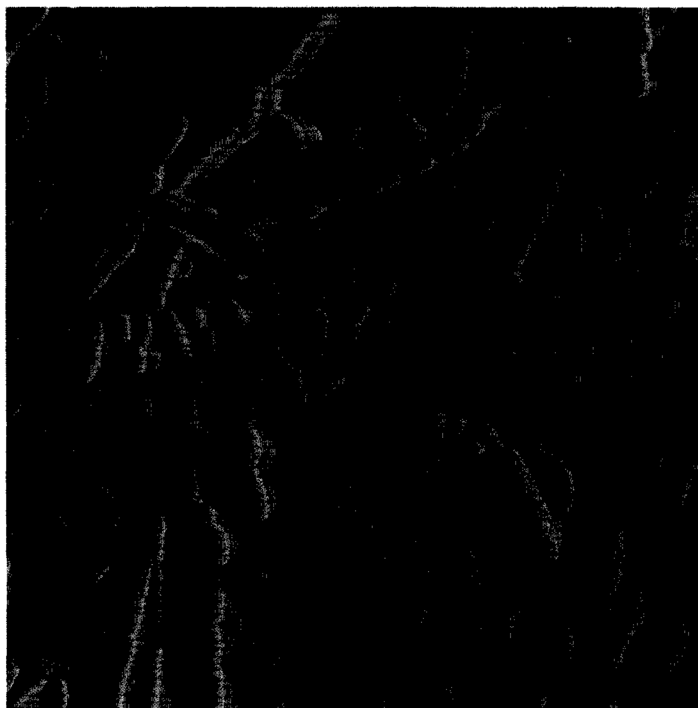

Figure 2.14. AFM image (3 μm × 3 μm) of pentacene films deposited onto mica at RT, with thickness of 70 nm.

2.5. Effect of Growth Conditions on the Morphology and Structure of Pentacene Thin Films

The previous sections discussed the nucleation and growth of pentacene thin films deposited at room temperature. However, according to the classical nucleation theory, the nucleation density depends on the diffusion of the material arrived on the substrate and the deposition rate. Thus, growth conditions, such as evaporation rate, nature of the substrate and substrate temperature, affect the nucleation of thin films, and their morphology, such as grain size, surface roughness, and crystal structure.

During the initial stages of the film growth, properties of the substrate play a crucial role. Basically, substrates can be divided into two groups: inert substrates and

Reproduced with permission of the copyright owner. Further reproduction prohibited without permission.

active substrates. Examples of active substrates are Si and metals. Glass and amorphous carbon are examples of inert substartes. Growth of pentacene films on Si(001) was studied by the IBM group (*Heringdorf, 2001*). Their results show that the thin-film phase is formed on Si(001). The strong interactions between dangling bonds of the substrate and individual pentacene molecules result in a flat lying (i.e. plane of the molecule is parallel with the substrate) wetting layer. Several STM studies have confirmed that sub-monolayer coverage of pentacene films on Si(001) and metal surface does indeed consist of flat lying molecules (*Kasaya, 1998; Hughes, 2002*). Above the wetting layer (i.e. films with more than one monolayer thickness), pentacene molecules stand up. In contrast, there is no wetting layer on inert substrates, and pentacene molecules (including the first layer) are oriented almost vertically to the substrate. Typically, the long axis of the molecule forms an angle of about 17° with respect to the surface normal (*C. Dimitrakopoulos, 1996*).

We deposited pentacene films onto amorphous carbon film and mica to investigate the effects of evaporation conditions, such as substrate temperature and evaporation rate, on the quality of these films. First, dependence of the grain size on deposition rate was observed. The pentacene films were deposited onto amorphous carbon film at rates of 0.5 Å/s and 1 Å/s at RT. The lateral crystallite dimensions are up to 0.2 μm at a deposition rate 1 Å/s (see Figure 2.15(b)) and can reach as high as 2 μm at a rate of 0.5 Å/s at RT (see Figure 2.15 (a)). While at 40 °C, the grain size up to 40 μm at a rate of 0.5 Å/s was observed (see Figure 2.15(c)). For comparison, pentacene films were deposited on mica at elevated temperature at a deposition rate of 0.5 Å/s. AFM images of the surface profiles are shown in Figure 2.16. Grain size up to

Reproduced with permission of the copyright owner. Further reproduction prohibited without permission.

20 μm both at 40°C and at 60°C was observed. The surface is flatter at 40°C and 60°C than at RT. Figure 2.17 shows XRD of pentacene films deposited at room temperature. At RT, we have measured the (001) inter-planar *d* spacing to be 15.29 Å (see Section 2.3), corresponding to "thin film phase". No other phases were observed by XRD in films grown at RT. In films grown at 40°C, a second phase often referred to as the "bulk phase" occurred with *d*(001*) *of* 14.33 Å together with "thin film phase" with *d*(001) of 15.24 Å (*Mattheus, 2003*). Peak positions, Miller indices and interplanar spacing are listed in Table 2.3. Films grown at 60°C also have the two above-mentioned phases and present strong "bulk phase".

Table 2.3. Measured data from XRD spectrum of pentacene thin films deposited on carbon at 40 °C. T, B mean thin film phase and bulk phase, respectively.

2-Theta [degree]	**Measured *d* [Å]**	**Miller indice (*hkl*)**
6.7	15.24	001 - T
7.2	14.33	001* - B
13.4	7.67	002 - T
14.2	7.24	002* - B
20.1	5.12	003 - T
21.5	4.78	003* - B
26.9	3.84	004 - T
33.8	3.07	005 - T

As described above, highly ordered films can be obtained even at room temperature. Decreasing the evaporation rate and increasing the substrate temperature can help to obtain larger grain size and flat surface. However, an elevated temperature may introduce polymorphs. It has been proved that in pentacene films coexistence of

Reproduced with permission of the copyright owner. Further reproduction prohibited without permission.

"thin film phase" and "bulk phase" can reduce the charge-carrier mobility (*Dimitrakopoulos, 2002*). So the growth conditions can affect the quality of pentacene film dramatically.

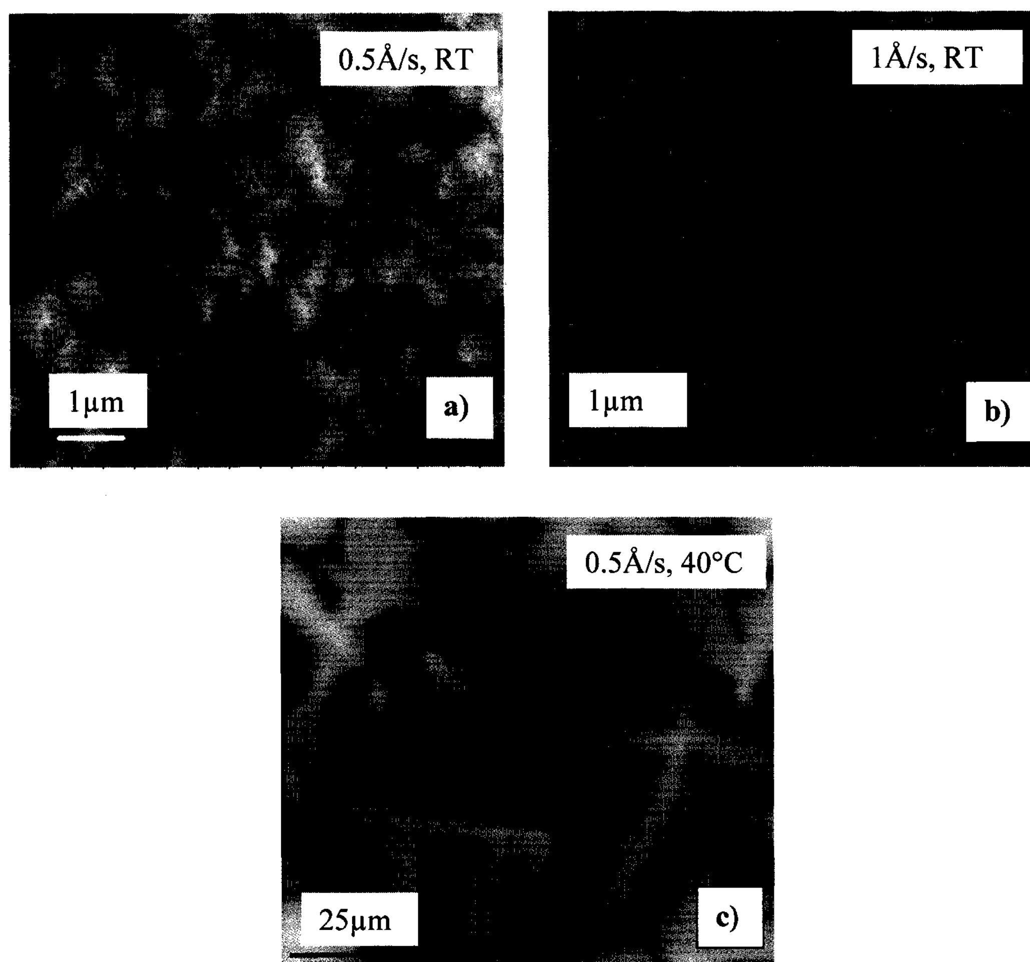

Figure 2.15. AFM images of pentacene films deposited on amorphous carbon foil a) at 0.5 Å/s at RT; b) at 1 Å/s at RT; c) at 0.5 Å/s at 40 °C.

Reproduced with permission of the copyright owner. Further reproduction prohibited without permission.

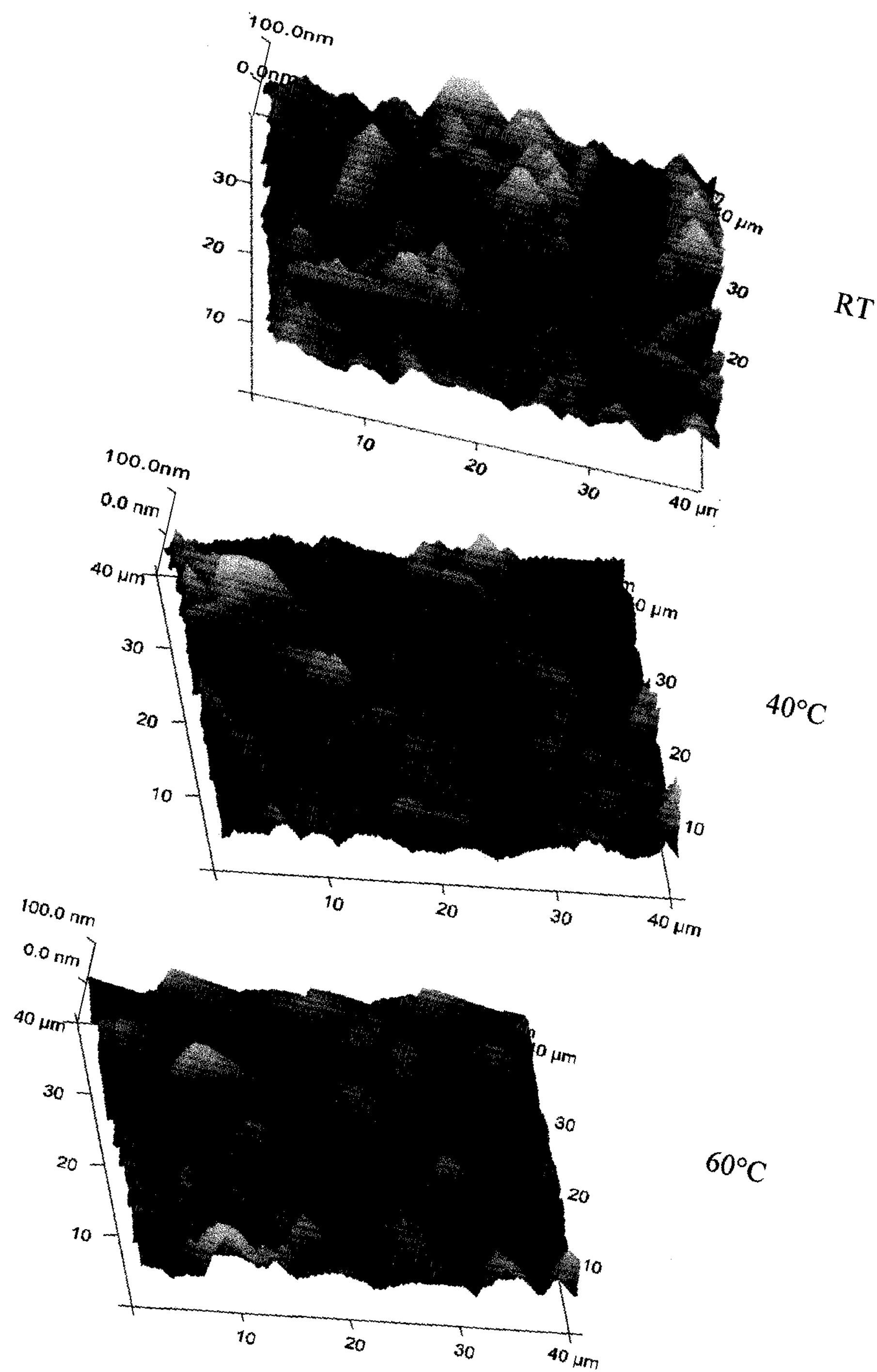

Figure 2.16. AFM images of surface plot of pentacene films deposited on mica at elevated temperatures.

Reproduced with permission of the copyright owner. Further reproduction prohibited without permission.

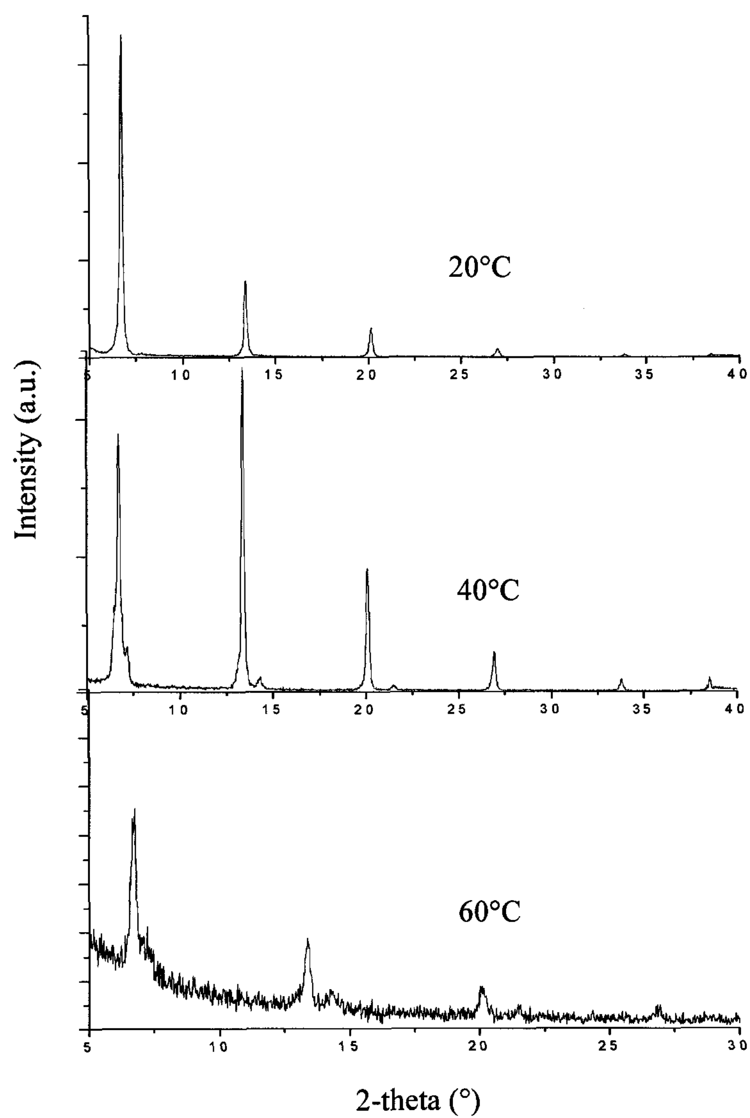

Figure 2.17. XRD spectra of pentacene films deposited on carbon foil at substrate temperature 20°C, 40°C and 60°C, respectively.

Reproduced with permission of the copyright owner. Further reproduction prohibited without permission.

2.6. Post Deposition Annealing of the Films

Thermal annealing is a common method to enhance film quality, such as suppressing the amount of crystal defects. To investigate the possibility of improving film quality, pentacene thin films deposited at RT were annealed in the growth chamber backfilled with argon to 1 atmosphere pressure. Due to the highly saturated vapor pressure of pentacene, it is not possible to anneal the films under vacuum because the films will quickly re-evaporate from the substrate. More precisely, pentacene films start to re-evaporate from the substrate surface at about 95 °C and the pentacene film will totally disappear if the time elapsed at the selected temperature (higher than 95 °C) is one-hour long even in chamber backfilled with argon gas. Figure 2.18 shows annealed pentacene films at 190 °C. In this case it took 20 minutes to heat the substrate to a desired temperature of 190 °C and the films were cooled in 30 minutes to room temperature with no dwell at 190 °C. Large, flat single crystals with lateral dimensions up to 1.5 μm formed, but not uniformly over the substrate area. The result of this experiment is shown in Figure 2.18(a).

In a second experiment, when the designed temperature (190°C) was reached, the film was held at that temperature for 15 minutes, then cooled within 60 minutes back to room temperature. The film presented discontinuous morphology and no larger single crystals were observed. The individual crystallites exhibited many bend contours and other defects.

Larger single crystallites can be obtained by flash (temperature increase in a short time and immediately cool down) annealing of pentacene films.

Reproduced with permission of the copyright owner. Further reproduction prohibited without permission.

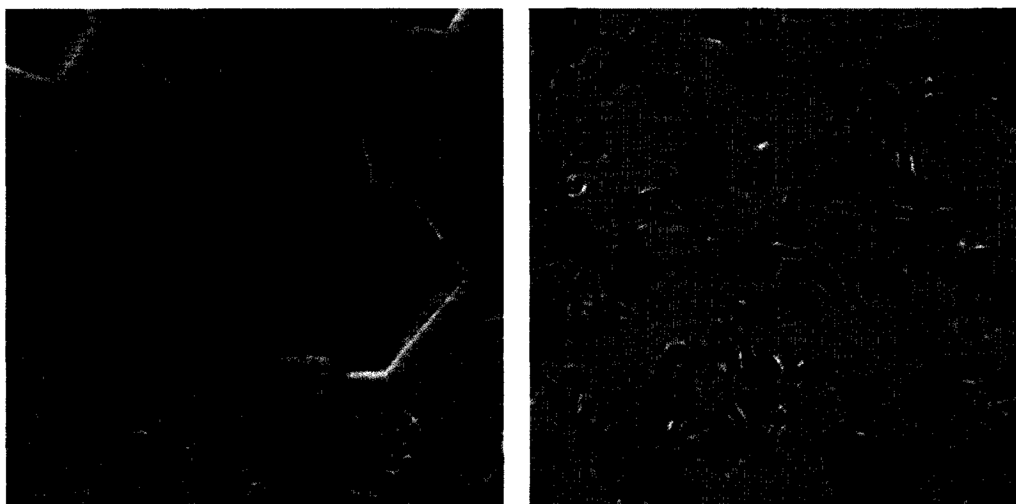

Figure 2.18. Pentacene films annealed at 190°C. Left: 30 minutes to cool to RT; right: constant temperature at 190°C for 15 minutes, then 60 minutes to cool to RT.

2.7. Conclusions

Ordered pentacene thin films, with their *ab* plane parallel to the substrate, can be obtained at room temperature by vacuum thermal evaporation. The "thin film phase" (interplanar spacing 15.3 Å) was observed in films grown on glass, Si and amorphous carbon. The growth process of pentacene films was observed and found to consist of four distinct stages. We observed that 2D islands with fractal-like shape transformed to 3D islands. At the same time the shape of the islands changed. This transition and change of island shape is believed to be the result of a reduction of surface energy. Adjusting the growth conditions can control the degree of crystalline ordering and the size of crystallites within polycrystalline films. Larger grains are obtained at the lower growth rates and higher substrate temperatures.

Reproduced with permission of the copyright owner. Further reproduction prohibited without permission.

Chapter 3. Electron Radiation Damage of Pentacene Thin Films Measured in TEM

3.1. Introduction

Pentacene, one of the candidates for large-area, mechanically flexible organic electronics (*Dimitrakopoulos, 2002*), stands out for its relatively high field-effect mobility (*T.N. Jackson, 1998*) and its ability to form well-ordered films on various substrates at room temperature. It is believed that molecule packing, grain size and morphology of thin films play a critical role in the performance of an organic electronic or electro-optical device. Therefore, it is imperative to study the microstructure of organic thin films relevant to electronics. However, electron irradiation damage limits the information obtainable by electron-beam techniques in beam-sensitive materials, particularly in organic specimens. Therefore, radiation damage of organic materials must be understood and quantified in order to ensure that the true structure of organic material is observed in electron microscopy experiments.

Radiation damage can be detected using a variety of characteristics of the sample. For example, mass-loss observed in TEM, changes in (optical) absorption spectra, decay of cathodoluminscence, fluorescence spectra and energy-loss measurement in the low loss region bear witness to radiation-induced changes. In the case of a crystalline sample in a TEM, a convenient measurement is to monitor the loss of crystallinity by observing the decay of sharp spots or rings in the electron diffraction pattern (loss of long-range order). Figure 3.1 shows a sequence of diffraction patterns of a pentacene film, acquired at progressively higher electron

Reproduced with permission of the copyright owner. Further reproduction prohibited without permission.

doses of 200 keV electrons in TEM. Along with this loss of the sharp diffraction rings, changes in morphology occur, as shown in the bright field TEM images in Figure 3.2. The loss of short-range order (damage suffered by individual molecules) can be seen from change in intensities of particular peaks in the electron energy loss spectrum. Quantitative measurement of peak intensity therefore offers a way to record the loss of short-range order.

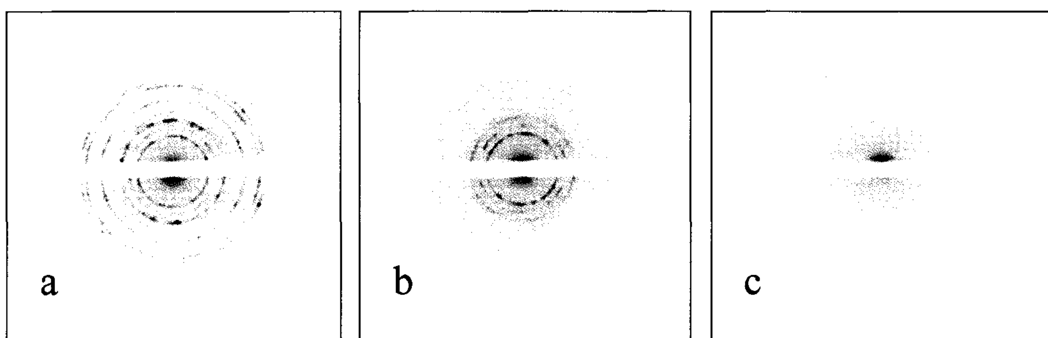

Figure 3.1. Crystallinity-loss as a function of irradiation dose D, for pentacene thin films irradiated at 200 kV in TEM.

Figure 3.2. Change in morphology observed in bright field images of pentacene films as a result of electron beam damage.

Reproduced with permission of the copyright owner. Further reproduction prohibited without permission.

The radiation response of a material is typically described in terms of the beam dose D, defined as the product of beam current density j and irradiation time t. To allow for comparison, one has to define the level of material response to this dose and two levels of material response were used in this work. The critical or end-point dose D_c is defined as the beam dose needed for complete disappearance of features of interest (such as rings in diffraction pattern). The measurement of end-point dose D_c is a subjective measurement since one has to visually estimate whether the feature of interest has disappeared. Therefore the end-point values may be somewhat inaccurate. To provide a more consistent method for comparing different possible responses to irradiation, the characteristic dose $D_{1/e}$ is preferable. Characteristic dose $D_{1/e}$ is defined as the dose required to decrease the intensity of a feature of interest (diffraction ring or edge in EELS spectrum) by a factor of 1/e. This dose can be measured quantitatively and may be related to a cross-section for radiation damage, corresponding to a specific damage mechanism, which in turn provides some insight as to what radiation damage mechanisms might be involved.

3.2. Experimental Methods

Pentacene thin films used for the radiation damage experiments were deposited onto TEM grids pre-coated with amorphous carbon (15 nm thick). The evaporation rate was 0.5 Å/s and the substrate temperature was RT. The thin films were uniform and the average thickness was 70 nm measured by EELS. The 70 nm film thickness was selected to represent the samples studied in Chapters 2 and 4 and to ensure that the films are sufficiently thin for EELS experiments. The instrument used to study radiation damage was a JEOL 2010 TEM, a 200 keV instrument equipped with LaB_6

Reproduced with permission of the copyright owner. Further reproduction prohibited without permission.

cathode, a CCD camera (suitable for both static and real-time observations) and a Gatan 666 parallel-recording electron energy-loss spectrometer. The experiments were carried at both room temperature and at liquid nitrogen temperature (measured to be about 90 K near the sample grid position) using Gatan 626 single-tilt cryogenic holder. The beam current I was measured by a TEM screen exposure meter calibrated using a Keithley 610 picoampermeter. The beam diameter d on the specimen was measured from the TEM screen, taking into account the microscope magnification M. The beam dose D corresponding to an exposure time t was then calculated as $D = (4IM^2/\pi d^2)t$. The diffraction patterns recorded on the CCD camera were processed off-line to obtain the integrated diffraction intensities for each ring. The background intensity was recorded after prolonged irradiation of the film and subtracted from each DP.

3.2.1. Loss of Long-Range Order Measured by Diffraction Pattern Fading

An example of a diffraction pattern of polycrystalline pentacene is shown in Figure 3.3. The $d(001)$ spacing in this particular pentacene thin film was 15.3 Å as measured by X-Ray diffraction (see Chapter 2), which agrees with published values for the thin-film phase (*Mattheus, 2003*). As shown in Figure 3.4, the intensity of each diffraction ring was integrated over all azimuthal angles using a Gatan DigitalMicrograph script. Lorentzian peaks were then fitted to match the intensity profiles to obtain the integrated intensity. Six intense rings, corresponding to (110), (200), (210), (220), (130), (320) reflections, were used to monitor the radiation damage, as shown in Figure 3.5.

Reproduced with permission of the copyright owner. Further reproduction prohibited without permission.

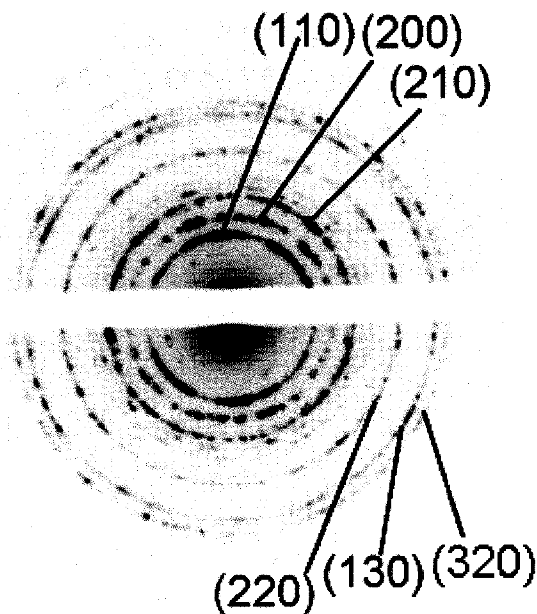

Figure 3.3. Diffraction pattern of polycrystalline pentacene thin films (70 nm) deposited onto amorphous carbon at RT.

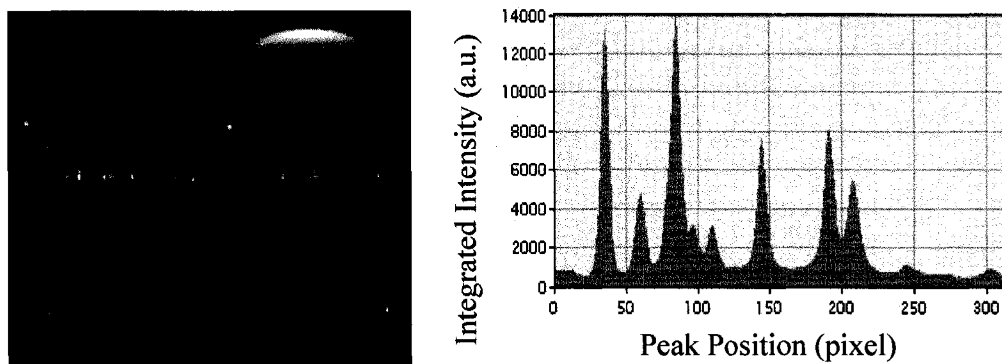

Figure 3.4. Left: integrated diffraction intensity over all azimuthal angles (0°-360°) of each ring; right: corresponding integrated Digital Micrograph profile.

Reproduced with permission of the copyright owner. Further reproduction prohibited without permission.

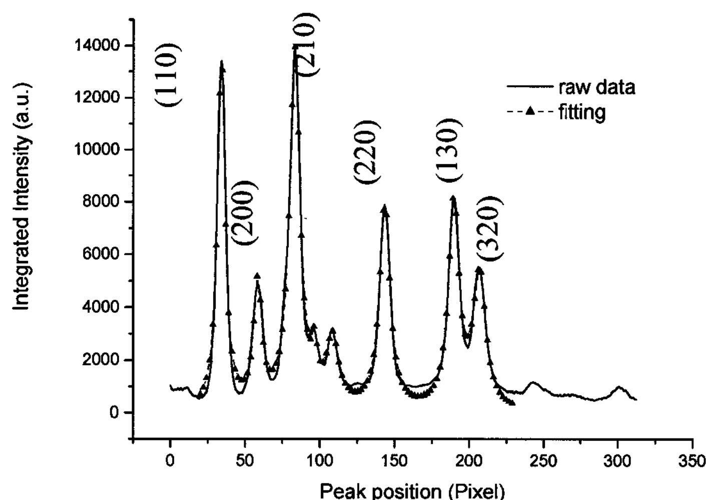

Figure 3.5. Peaks corresponding to (110), (200), (210), (220), (130) and (320) reflections were fitted using Lorentzian function.

3.2.2. Loss of Short-Range Order Measured by Electron Energy Loss Spectroscopy

Electron energy-loss spectra were recorded using a Gatan-666 parallel recording spectrometer. A large energy dispersion (0.05 eV/channel) of the spectrometer was employed to record the plasmon resonance of the π-electrons, a characteristic feature of aromatic ring structures. Figure 3.6 shows low-loss region spectrum of the pentacene thin film. Three peaks were observed at ~7 eV, ~ 8.7 eV and ~ 11.8 eV from the same specimen in different regions. The amorphous-carbon substrate was measured to ensure there is no feature in the region of interest and that the observed features originated from the pentacene film. In our experiments the 7 eV peak was rarely seen, whereas 8.7 eV and 11.8 eV peaks appeared in all samples.

Reproduced with permission of the copyright owner. Further reproduction prohibited without permission.

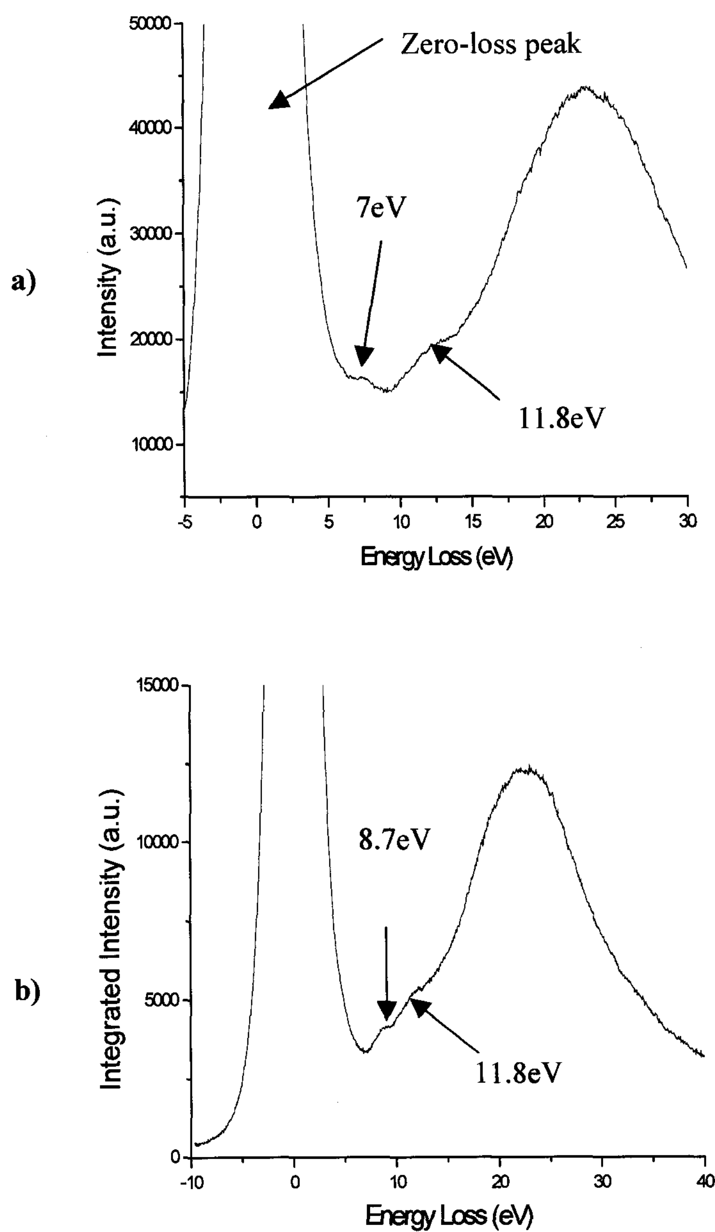

Figure 3.6. π-Excitation peaks in the energy loss spectrum of pentacene.

Reproduced with permission of the copyright owner. Further reproduction prohibited without permission.

The pentacene thin films with a thickness of 70 nm were irradiated using a constant beam size (3 μm at the sample plane). The beam-current density (also known as dose rate) j was controlled by varying the total beam current I by changing the TEM filament temperature. We monitored the decay of 7 eV and 8.7 eV peaks at room temperature or at liquid-nitrogen temperature (T = 90 K). The end-point doses were obtained by measuring the complete disappearance of both 7 eV and 8.7 eV peaks with increasing beam dose.

3.3. Discussion of Experimental Results

3.3.1. Loss of Long-Range Order Observed in Diffraction Patterns

In order to obtain the characteristic beam dose $D_{1/e}$ or the end-point dose D_c, a series of experiments of radiation measurement in terms of the decay of diffraction rings were carried out as described above. To find out whether the damage process is dependent on dose rate, the intensity of the (110) reflection with spacing d = 4.7 Å, (*Wu, 2004; Drummy, 2003*), was monitored as a function of radiation dose D at several beam current densities j. The dose rate can be independently controlled, either by changing the incident beam diameter or by changing the total incident beam current I. Experiments were performed to isolate the effects of these two parameters from each other. Dose rates j from 0.6×10^{-3} A/cm^2 to 6.2×10^{-3} A/cm^2 were used in our experiments. At higher dose rates, the damage proceeds too fast to be monitored using our camera.

Reproduced with permission of the copyright owner. Further reproduction prohibited without permission.

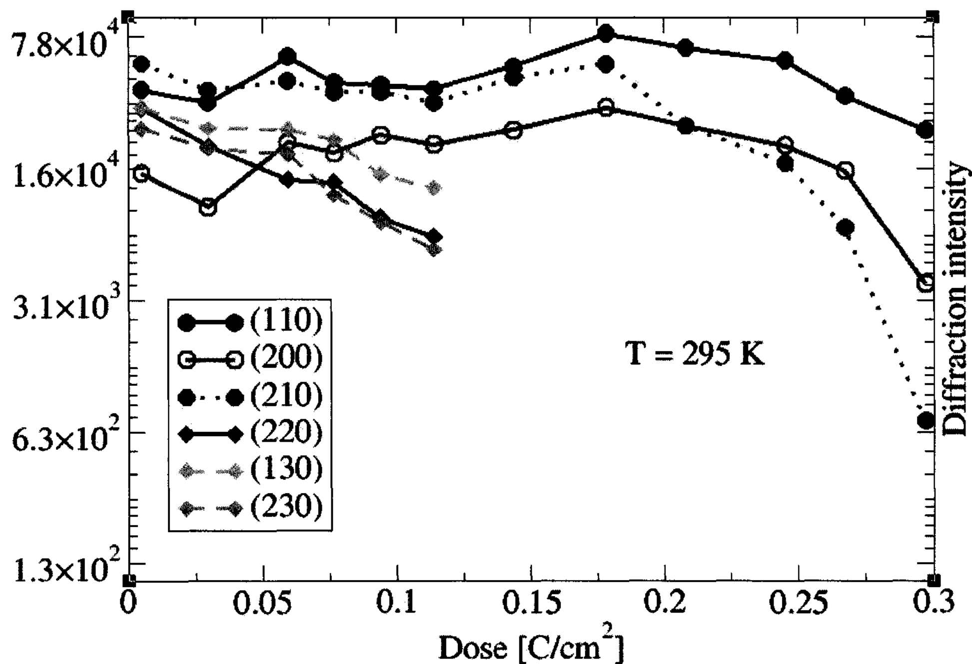

Figure 3.7. Fading of diffraction rings monitored at room temperature with dose rate j = 0.6×10^{-3} A/cm^2.

At room temperature, we observed that the integrated intensity first increased and then decreased with increasing beam dose. At 90 K, the integrated intensity remained unchanged or exhibited a small change. Both at room temperature and 90 K, a "latent dose" effect, in which no change in the diffraction intensities occurred for as much as 50% to 60% of the exposure (*Glaeser, 1978*) was observed. Because the damage process is a non-exponential decay, the value of $D_{1/e}$ was calculated using the data measured as the diffracted intensity first decreased and then disappeared. Examples of changes in diffraction intensities are shown in Figures 3.7 and 3.8, measured at room temperature and at 90 K, respectively. The measured values of end-point dose and characteristic dose are listed in Table 3.1.

Reproduced with permission of the copyright owner. Further reproduction prohibited without permission.

Table 3.1. Characteristic and end-point doses at various dose rates j measured by fading of (110) diffraction ring, both at room temperature and at 90 K.

Temp. [K]	**Beam diameter [μm]**	**Beam current [nA]**	**Dose rate j [A/cm^2]**	**Characteristic dose $D_{1/e}$ [C/cm^2]**	**End-point dose Dc [C/cm^2]**
295	3	0.04	0.60×10^{-3}	0.10±0.02	0.44±0.04
	2		1.08×10^{-3}	0.09±0.03	0.52±0.03
	1		4.33×10^{-3}	0.15±0.04	0.78±0.01
	3	0.13	1.88×10^{-3}	0.18±0.06	0.62±0.04
		0.07	0.95×10^{-3}	0.14±0.03	0.53±0.04
90	3	0.19	2.50×10^{-3}	0.56±0.08	1.80±0.04
	2		6.20×10^{-3}	0.55±0.09	2.20±0.01
	3	0.32	4.30×10^{-3}	0.50±0.08	2.42±0.04

Although $D_{1/e}$ is independent of dose rate as expected, an apparent increase in the end-point dose D_c with dose rate was observed at room temperature. There was no dependence of $D_{1/e}$ on beam size. For the room temperature data, the initial increase of diffraction intensity (latent dose) can be explained in terms of a larger crystallite volume (under dynamic diffraction conditions) breaking into smaller crystallites, which provide kinematic diffraction conditions (*Reimer, 1965*), or in terms of the crystallites reorienting to be closer to Bragg condition for some reflections due to the heating by the electron beam. At low temperature, the original structure may be "frozen in" during at least half of the critical exposure.

Reproduced with permission of the copyright owner. Further reproduction prohibited without permission.

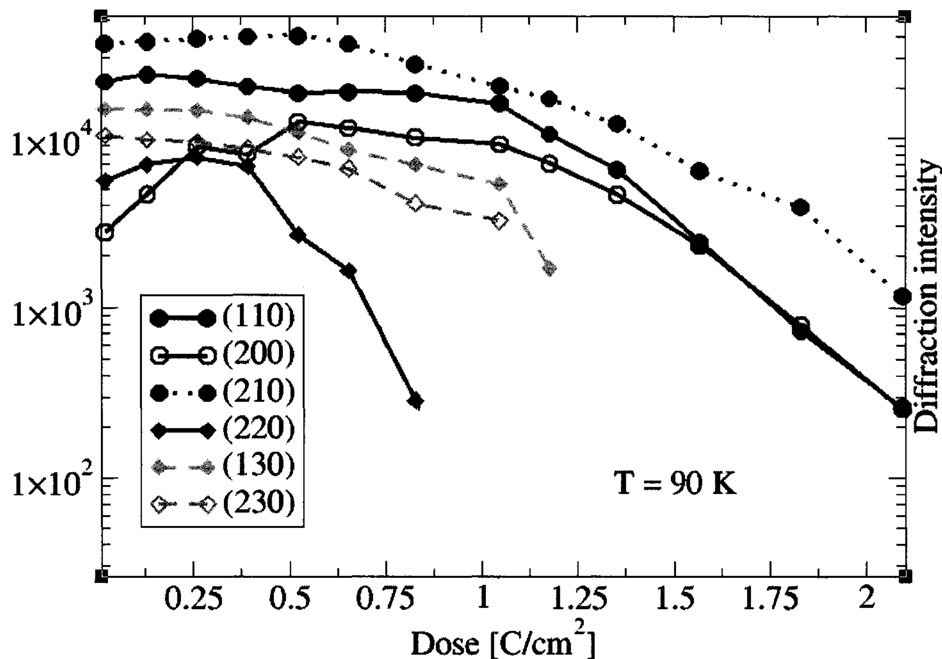

Figure 3.8. Fading of diffraction rings with beam dose measured at liquid-nitrogen cooling temperature 90 K with dose rate $j = 4.3\times10^{-3}$ A/cm^2.

From Table 3.1 we can see that the characteristic dose $D_{1/e}$ (~0.5 C/cm^2) at 90 K was about 3 times of that at room temperature (0.1~0.15 C/cm^2). The end-point dose at 90 K was larger than at 295 K by a factor of three, confirming that cooling a sample can reduce the loss of long-range order.

From Figure 3.7 and Figure 3.8, we can see the outer rings (with smaller d spacing) vanish faster than the inner rings (with larger d spacing). This might be explained by initial distortion of short distances by cross-linking (*Reimer, 1965*). The end-point doses D_c and $D_{1/e}$ for each ring in the DP are listed in Table 3.2.

Reproduced with permission of the copyright owner. Further reproduction prohibited without permission.

Table 3.2. Characteristic dose $D_{1/e}$, end-point dose D_c and latent dose for each DP ring measured at 295 K and 90 K.

Temp. [K]	**Dose rate *j* [A/cm²]**	**Miller index**	**Latent dose D_L [C/cm²]**	**Characteristic dose $D_{1/e}$ [C/cm²]**	**End-point dose D_c [C/cm²]**
295	0.6x10⁻³	110	0.18	0.1	0.45
		200	0.18	0.06	0.45
		210	0.18	0.03	0.45
		220	< 0.03	0.07	0.14
		130	< 0.03	0.11	0.14
		320	< 0.03	0.07	0.14
90	4.3x10⁻³	110	1.1	0.5	2.4
		200	~1	0.4	2.4
		210	0.7	0.5	2.4
		220	NA	0.3	1.2
		130	< 0.3	0.6	1.2
		320	< 0.1	0.85	1.2

3.3.2. Loss of Short -Range Order Observed in EELS Measurement

Table 3.3 lists values of the end-point doses for the fading of the 8.7 eV peak at room temperature and at $T = 90$ K. The end-point dose measured at $T = 90$ K is not different from that measured at room temperature, which suggests that the mechanism responsible for loss of short range order is independent of temperature. At higher dose rate a higher end-point dose was observed.

Reproduced with permission of the copyright owner. Further reproduction prohibited without permission.

Table 3.3. End-point dose for fading of 8.7 eV peak, measured for pentacene at room temperature and at 90 K.

Temperature [K]	Dose rate [A/cm^2]	Beam diameter [μm]	End-point dose [C/cm^2]
295	0.6×10^{-3}	3	0.20±0.04
	1.0×10^{-3}	3	0.31±0.03
90	0.5×10^{-3}	3	0.24±0.05
	1.1×10^{-3}	3	0.32±0.02

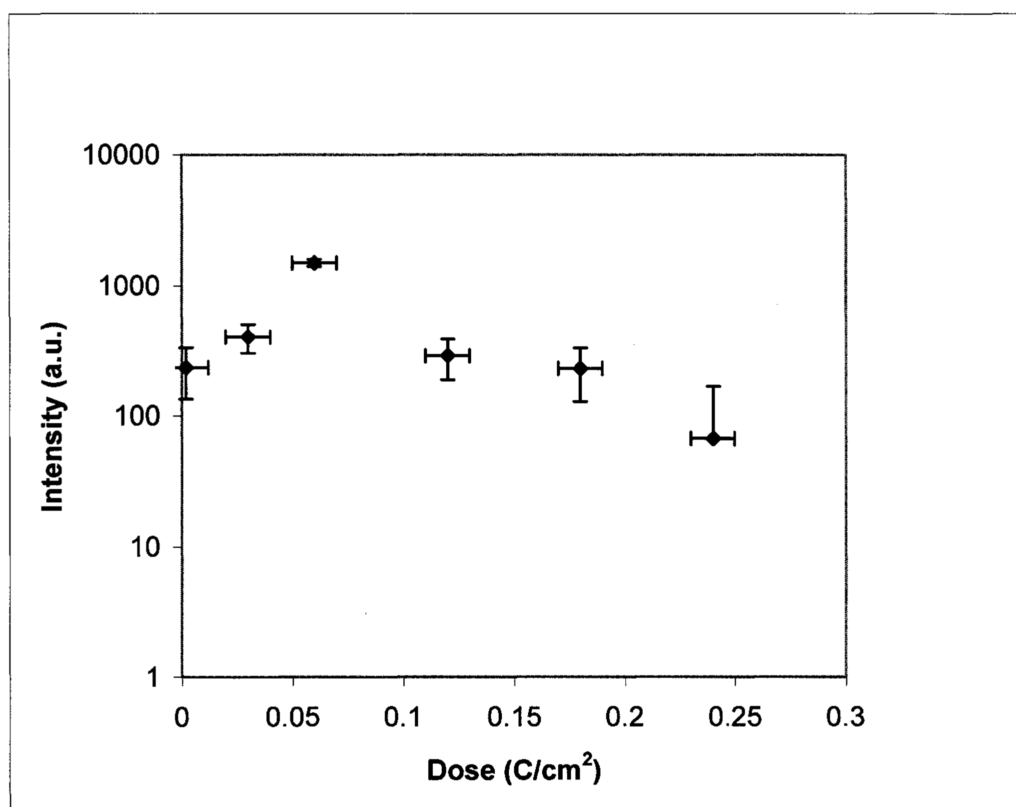

Figure 3.9. The intensity of 7 eV peak of pentacene thin films versus beam dose measured at room temperature.

We also monitored the 7 eV peak at a dose rate of 0.6×10^{-3} A/cm^2 with beam probe diameter of 3 μm at room temperature. The dependence of intensity of the 7 eV

Reproduced with permission of the copyright owner. Further reproduction prohibited without permission.

peak on beam dose D is plotted in Figure 3.9. The intensity of the 7 eV peak initially increased, and then decreased. The characteristic dose was calculated using the decreasing part of the dependence, and a value of $D_{1/e}$ = 0.06 C/cm^2 was obtained. A possible explanation for the initial increase of intensity of the 7 eV peak is the rupture of C-H bonds and of side chains (*Reimer, 1965*).

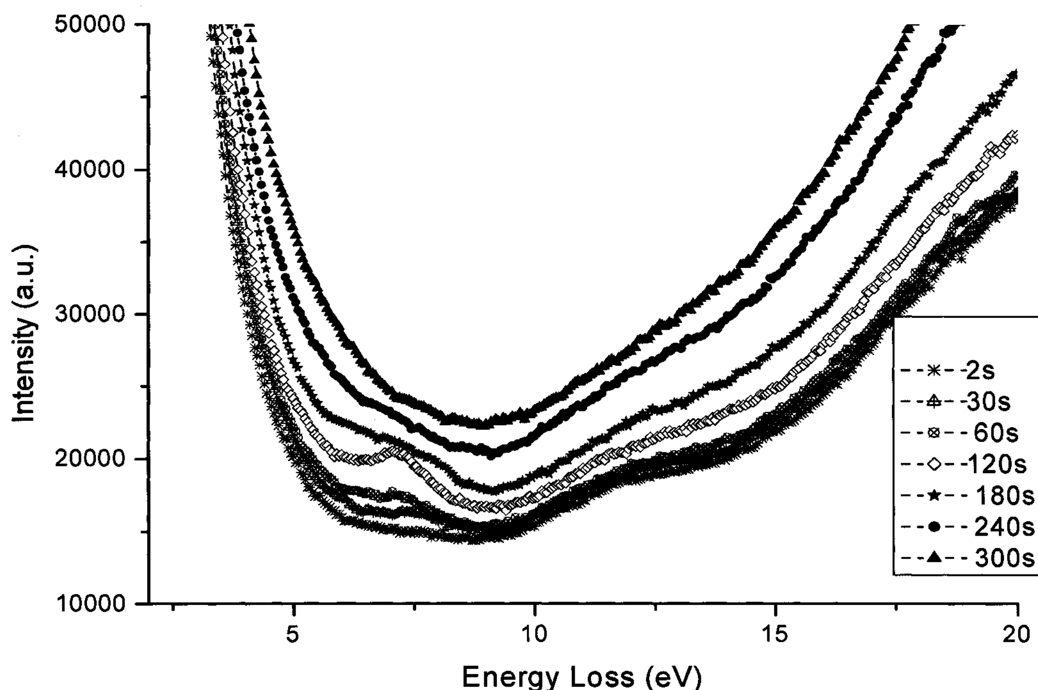

Figure 3.10. Series of low-loss spectra of pentacene measured at selected time intervals.

The intensity of both zero-loss peak (ZLP) and plasmon peak increased with beam dose during the above experiments, as can be seen in Figure 3.10. The logarithm of total intensity of ZLP and plasmon peak over the intensity of ZLP (t/λ) was plotted versus beam dose, shown in Figure 3.11, which allowed us to estimate change of mass

Reproduced with permission of the copyright owner. Further reproduction prohibited without permission.

thickness within the irradiated area. The data correspond to a thickness increase of about 12%. This mass gain might be due to hydrocarbon contamination and diffusion of fragments of pentacene molecules towards the electron beam (*Egerton,* 2004). In general, the escape rate of secondary electrons is not compensated by arrival of conduction electrons in the sample, resulting in electrostatic field in vicinity of the irradiated area. It is possible that electrostatic field resulting from electron beam irradiation increases the diffusion of such fragments and contamination to the irradiated area.

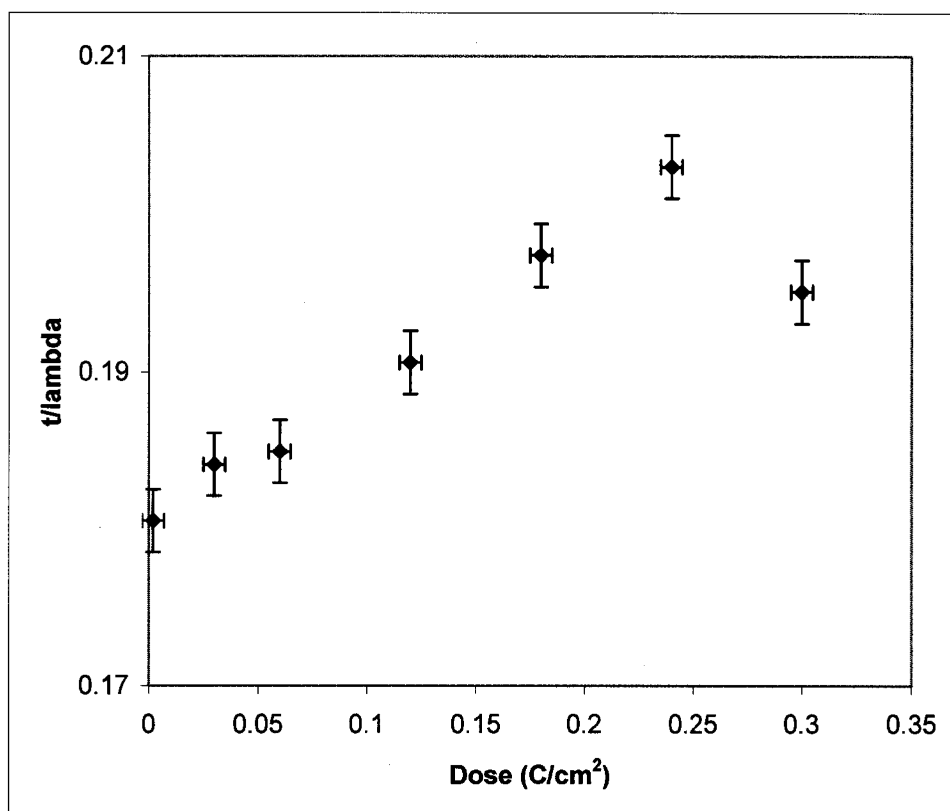

Figure 3.11. Logarithm total intensity of ZLP and plasmon region over the intensity of ZLP versus beam dose.

Reproduced with permission of the copyright owner. Further reproduction prohibited without permission.

3.4. Discussions of Electron-Beam-Induced Radiation Damage in Pentacene

In this Section we wish to assess the relation between the observed DP damage behavior, the valence-peak damage behavior and the rate of carbon-atom K-ionization and valence-electron excitation. The cross-sections $\sigma = q/D_{1/e}$, where q is the electron charge, were calculated for inelastic scattering, due to both carbon K-shell excitation and valence-electron excitation. The cross-section σ for C-K was calculated with the SIGMAK3 program using relativistic kinematics and a hydrogenic model (*Egerton, 1996*). The cross-section for valence electrons was measured from the measured plasmon energy E_p = 23.6 eV and the FWHM of the plasmon resonance ΔE_p = 16.7 eV using

$$\sigma_{tot}^{val} = \frac{1}{\pi a_0 m_0 v^2 n_a} \int_0^{E_0} \left(\ln[\theta_E^2 + 2\theta_E] - \ln[\theta_E^2] \right) \Im\left(-\frac{1}{\epsilon(E)} \right) dE \quad , (3\text{-}1)$$

where the imaginary part of dielectric function $\varepsilon(E)$ is

$$\Im\left(-\frac{1}{\epsilon(E)} \right) = \frac{E \Delta E_p E_p^2}{(E^2 + E_p^2)^2 + (E \Delta E_p)^2} \,. \quad (3\text{-}2)$$

In the Equation (3-2), a_0 is Bohr radius, E_0 incident energy, m_0 electron mass, v electron velocity and n_a number of atoms per unit volume. These calculated $D_{1/e}$ values have been converted to a $D_{1/e}$ per pentacene molecule, by multiplying the cross-section per atom by the number of 22 for C 1s and 36 for valence shells (*Egerton, 2004*). The calculated values are listed in Table 3.4.

Reproduced with permission of the copyright owner. Further reproduction prohibited without permission.

Table 3.4. Calculated damage characteristic doses per molecule.

C 1s σ_k [$cm^2 \times 10^{-19}$]	**Valence-electron σ_v [$cm^2 \times 10^{-19}$]**	**C 1s $D_{(1/e,k)}$ [C/cm^2]**	**Valence-electron $D_{(1/e,v)}$ [C/cm^2]**
3.41	1068	0.47	1.5×10^{-3}

The π bond or σ bond degradation behavior in pentacene cannot be counted for inelastic scattering of incident electrons by valence electron excitation by comparing the measured with calculated cross-sections. As shown in Table 3.5, the measured $\sigma_{(Dc)}$ for 7 eV and 8.7 eV peak destruction are about 2 orders of magnitude lower than the calculated σ_v. In contrast, the measured damage cross-section $\sigma_{(Dc)}$ are in the same order of magnitude as the calculated σ_k. Thus, the carbon K shell ionization could be responsible for valence electron change. Moreover, the measured DP damage $\sigma_{(Dc)}$ are in the same order of magnitude as the calculated DP σ_k. Therefore, the damage mechanism in pentacene is likely related to C-K shell excitation.

Table 3.5. Measured damage cross-sections using the end-point dose both for DP (110), (320) plane and EELS 7 eV, 8.7 eV peak destruction.

Temperature	**Method**	**Features**	**D_c [C/cm^2]**	**Cross section $\sigma_{(Dc)}$ [$cm^2 \times 10^{-19}$]**
RT	DP	(110)	0.44	3.64
		(320)	0.14	11.4
	EELS	7 ev	0.25	6.4
		8.7 ev	0.20	8.0
90 K	DP	(110)	2.7	0.59
		(320)	1.2	1.3

Reproduced with permission of the copyright owner. Further reproduction prohibited without permission.

Chapter 4: Optical Properties of Pentacene Thin Films

4.1. Introduction

Organic semiconductors have received a great deal of interest due to their extensive applications in the fields of electronics and optics. These applications include chemical, physical and biological sensors, microelectronic devices, non-linear optical and molecular devices (*Forrest, 2000*). One example is the practical realization of a range of integrated organic devices, which are perhaps best exemplified by the vertically stacked, full-color organic light-emitting devices for flat panel displays. This device emits the red (R), green (G), and blue (B) primary colors through intervening transparent contacts and organic films developed specifically for this purpose. Passing current through the appropriate layers independently energizes each of the R, G, and B sub-pixels. Electrically induced excitons (excited states of a molecule) emit light of a particular color, depending on the molecular structure and composition of that layer. However, after more than fifty years of research in organic semiconductors, there is still much that is unknown about their basic properties, such as how they grow in ordered layers and the nature of their excited states. Pentacene, as discussed in Chapter 1, is a promising material among organic semiconductors due to its high charge carrier mobility and switching on/off ratio. However, the relation of some of the basic physical properties of pentacene films to their morphology is still not well understood.

Many aromatic compounds (including pentacene) contain double or even bonds between their carbon atoms and often give rise to strong luminescence emission. This luminescence originates from the excited states of the delocalized π-electrons in

Reproduced with permission of the copyright owner. Further reproduction prohibited without permission.

these molecules when the excitation source is applied. Figure 4.1 shows the luminescence process that can occur in the π-electron system of an organic molecule. All π-electron systems contain an even number of π-electrons since there are two electrons per π-bond. In ground state, since the electron spins will be paired off, any π-electron system is a singlet state S_0. If the π-electrons are excited without change of spin, the resultant excited states are also singlet states. However, if the excited π-electron suffers a spin reversal between the ground and excited state, the resultant excited state is a triplet state.

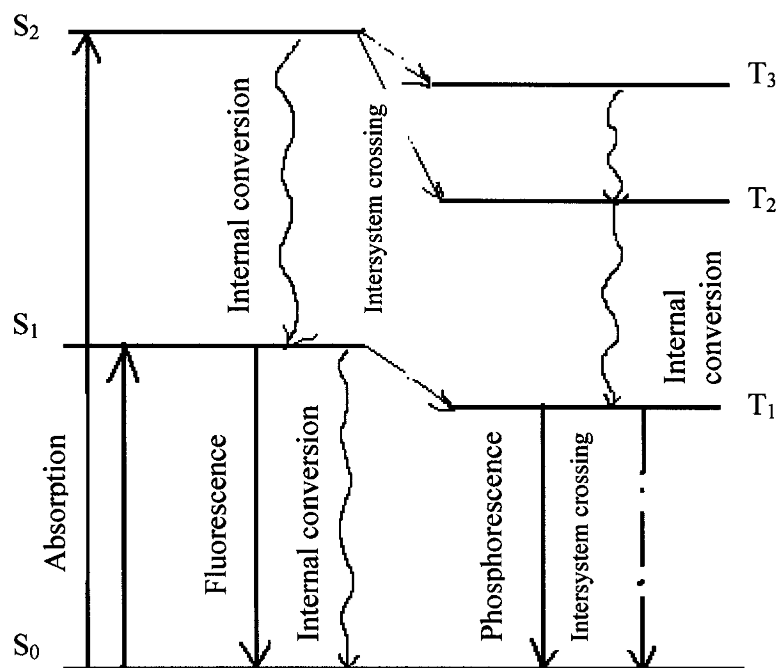

Figure 4.1. π-electron luminescence process (Lumb, 1978).

Luminescence may be produced by absorption into any of the excited singlet state S_1, S_2, S_3...etc. However, the primary fluorescence emission generally occurs from the lowest excited singlet state S_1 irrespective of the initial state excited.

Reproduced with permission of the copyright owner. Further reproduction prohibited without permission.

Radiative transitions from the higher excited states are very weak due to the efficient and rapid non-radiative process of internal conversion between S_2, S_3,...etc and the lowest excited state S_1 (*Lumb, 1978*).

Non-radiative process, such as internal conversion, intersystem crossing, takes place between energy states without emission of light. Intersystem crossing is the non-radiative transfer of energy from the singlet manifold to the triplet manifold. The rate constant for intersystem crossing and internal conversion decreases with the increase in energy gap between the respective electronic states. Internal conversion occurs in the triplet manifold and a molecule excited into a higher triplet, such as T3, will rapidly internally convert to the lowest triplet state T1. The probability of radiative emission from T_1 to S_0 will then compete with the non-radiative intersystem crossing from T_1 to S_0. Intrinsically, phosphorescent emission of light occurs. The lifetime of T1 is usually of the order of seconds and decreases as the energy gap decreases since transitions, radiative or non-radiative, between T_1 and S_0 are formally forbidden. Therefore, the long-lived phosphorescence is at longer wavelength than the corresponding fluorescence emission. This is a generic case, not specific to pentacene.

In this chapter, the optical UV absorption and photoluminescence of pentacene films will be discussed. Optical properties calculated from measured low-loss data in electron-energy loss spectrum will also be covered.

Reproduced with permission of the copyright owner. Further reproduction prohibited without permission.

4.2. Optical Absorption and Photoluminescence Measurement

4.2.1. Experimental

Optical measurements were made on pentacene films deposited onto optical grade fused quartz wafers and Si(001) cleaned in Piraha first and then dipped in HF (1 minute). The films were grown at room temperature at an evaporation rate of 1 Å/s, with thickness of 70 nm, 100 nm and 120 nm, respectively. For measurements of the optical absorption spectra of the films, light from a deuterium–tungsten lamp was coupled into an optical fibre for illuminating the films at normal incidence. The light transmitted through the samples was then collected by a second optical fibre and analyzed using a CCD spectrometer (Ocean Optics) whose sensitivity was normalized with respect to a standard black body radiator. PL spectroscopy was done using the 325 nm line of a HeCd laser as the excitation source (20 mW). The PL of pentacene films on Si wafer was reflectively collected and analyzed using two CCD spectrometers (one is sensitive to wavelength from 200 nm up to 800 nm and the other is from 500 nm up to 1200 nm). All the measurements were done at room temperature.

4.2.2. Results of Absorption Measurement

Figure 4.2 shows absorption spectra of pentacene films deposited onto fused quartz at room temperature. Strong peaks are observed in the near infrared and visible region, positioned at 1.85 eV (670 nm) with additional fine peaks at 1.94 eV (639 nm), 2.11 eV (588 nm) and 2.28 eV (544 nm), and in the far-ultraviolet region, positioned at 4.50 eV (276 nm), 5.4 eV (broad), and 6.33 eV. The absorption spectra in the low energy region of our polycrystalline pentacene films did not vary from film to film and

Reproduced with permission of the copyright owner. Further reproduction prohibited without permission.

were similar to those reported in the literature (*Lee, 1977; Park, 2002*). It is characteristic for organic aromatic solids to exhibit a "solvent" red shift of absorption spectra in the solid phase compared to gas phase or solution environment. This shift is due to the change in the dielectric and optical properties of the crystal from the vapor or liquid environment, and the interaction of the excited molecules with equivalent adjacent molecules (*Lumb, 1978*). In our pentacene films, the lowest excitation is at 1.85 eV (670 nm), corresponding to a shift of 0.31 eV (95 nm) with respect to the solution spectrum of pentacene in benzene from literature (*Lee, 1977*).

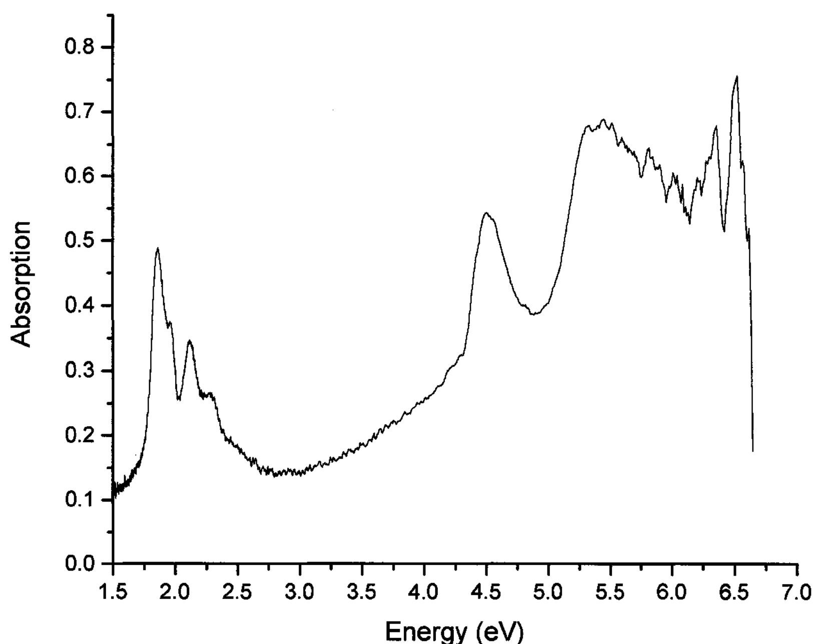

Figure 4.2. Measured absorption spectrum of pentacene thin films deposited onto fused quartz at RT.

Another feature is Davydov splitting observed in our pentacene films at room temperature. Davydov splitting occurs in crystals where there is more than one

Reproduced with permission of the copyright owner. Further reproduction prohibited without permission.

inequivalent molecule per unit cell. The energy state splits into as many components as there are inequivalent sites. This Davydov splitting is a few hundred cm^{-1} for singlets and about tens of cm^{-1} for the triplet states (*Davydov, 1971; Lumb, 1978*). In the case of pentacene, there are two herringbone-arranged molecules per unit cell. The splitting of the first electronic excitation in single pentacene crystal is about 1000 cm^{-1} (with $\perp$b component of 1.97 eV (15900 cm^{-1}) and $\parallel$b component of 1.83 eV (14750 cm^{-1}) (*Davydov, 1971*). As shown in Figure 4.2, the lowest doublet energy bands in our polycrystalline pentacene film spectra are approximately at 1.85 eV (14930 cm^{-1} termed *b*-component) and 1.94 eV (15650 cm^{-1} termed *a*-component) corresponding to the single crystal Davydov $\parallel$b and $\perp$b components, respectively. The splitting is about 0.1 eV (720 cm^{-1}) corresponding to singlet state excitation (S_0-S_1).

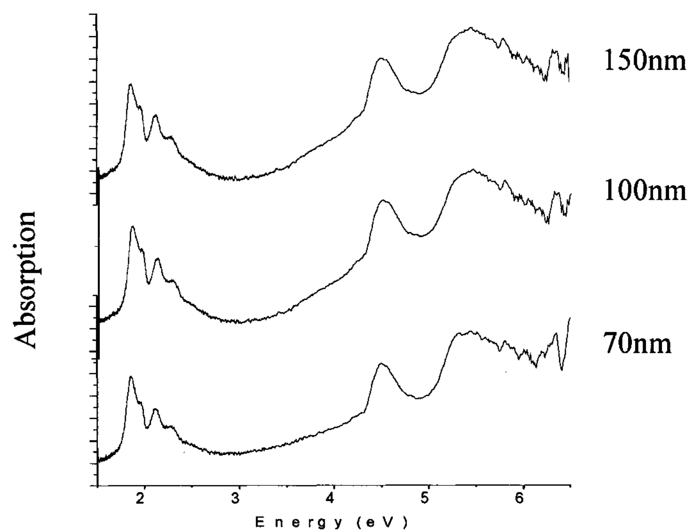

Figure 4.3. Absorption spectra of pentacene films, deposited at room temperature as a function of thickness.

Reproduced with permission of the copyright owner. Further reproduction prohibited without permission.

One more observation is that the absorption spectra of pentacene films are not thickness dependent. The absorption spectra of films of varying thickness, all deposited under the same conditions, are shown in Figure 4.3. The band features appear to be similar in all the spectra.

4.2.3. Photoluminescence Measurement

From our PL measurement, the emission peaks are positioned at 1.27 eV (973 nm), 1.40 eV (884 nm), 1.76 eV (705 nm), 1.86 eV (665 nm), 2 eV (620 nm), and 3.16 eV (392 nm), as shown in Figure 4.4. The emission spectrum is shifted to longer wavelengths with respect to the absorption spectrum. However, we assigned the lowest energy band gap in pentacene films as 1.85 eV based on absorption spectrum, so the peak of 705 nm (1.76 eV) might correspond to S_1-S_0 emission, if the Stokes shift (0.09 eV) is considered. Although the primary fluorescence emission occurs from the lowest excited singlet state irrespective of the initial state excited, radiative transitions from the higher excited states were also observed in our measurement. We assign peaks at 1.27 ev and 1.40 eV as phosphorescence. There is a strong PL peak centered at 3.16 eV (392 nm) whose FWHM is about 1 eV, as shown in Figure 4.4(a).

4.3. Optical Properties Calculated from Electron-Energy Loss Spectrum

The low-loss region (<50 eV) of EELS also contains information on the optical properties of materials. The predominant features in this part of the spectrum are the plasmon peaks, which represent the response of the weakly bound valence and conduction electrons to the high-energy incident electron. The plasmon response contains direct information about the free-electron density (*Egerton, 1996*). From the

Reproduced with permission of the copyright owner. Further reproduction prohibited without permission.

low-loss region, we can obtain the dielectric function of the specimen. In the region of the spectrum immediately after the zero-loss peak and before the rise in intensity preceding the plasmon peak, several low intensity peaks can be seen. From this region we can discern certain inter-/intra- band transitions, especially in polymers, and can measure the band gap of the semiconductor and insulators.

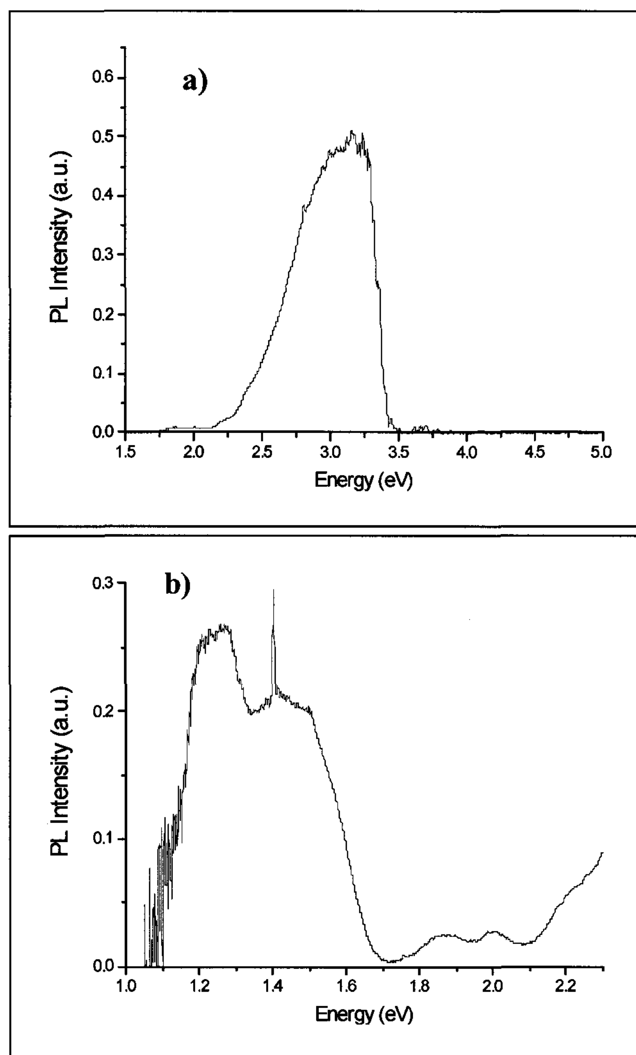

Figure 4.4. PL spectra of pentacene films deposited onto Si(001) wafer at RT.

Reproduced with permission of the copyright owner. Further reproduction prohibited without permission.

4.3.1. EELS Spectrum Measurement

Pentacene thin films were deposited onto TEM grids (pre-covered with 15 nm-thick amorphous carbon) at room temperature, to a thickness of 70 nm. The low-loss spectrum was obtained using incident electron energy of 200 keV, a collection angle 5 *mrad*, and the spectrometer energy dispersion of 0.05 eV/channel. In order to minimize electron-beam damage to the specimen, the incident beam was defocused to 3 μm in diameter, keeping the total dose in the measured area less than 1.2×10^{-3} C/cm^2, which is about two orders of magnitude smaller than the end-point dose to damage the molecules (discussed in Chapter 3). Figure 4.5 shows a low-loss region spectrum of pentacene. The FWHM of the zero-loss peak is 1.2 eV.

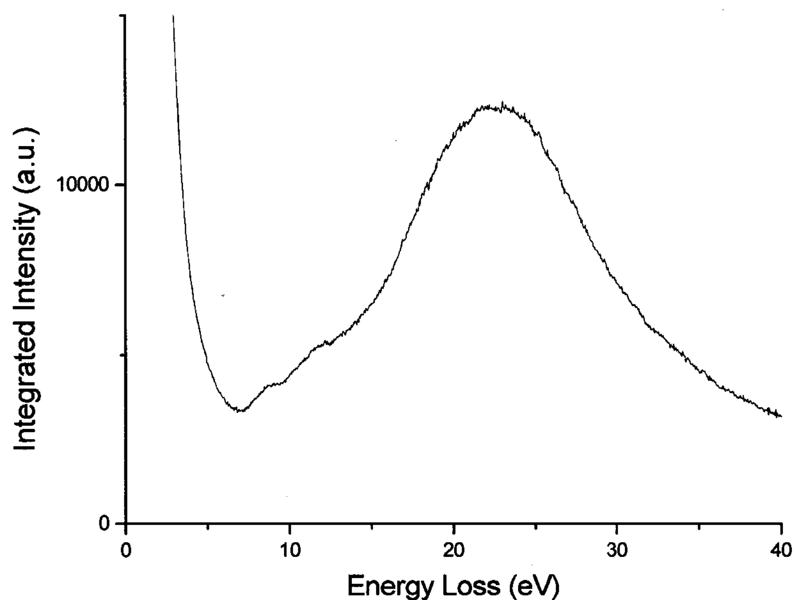

Figure 4.5. Low-loss region spectrum of 70 nm thick pentacene films, deposited onto amorphous carbon at RT.

Reproduced with permission of the copyright owner. Further reproduction prohibited without permission.

4.3.2. Calculation of Optical Constants

The single-scattering distribution is related to the complex permittivity $\varepsilon(E)$ of the specimen. From the single-scattering distribution, Kramers-Kronig (K-K) analysis enables the energy dependence of the real and imaginary part (ε_1 and ε_2) of the permittivity to be calculated. This in turn allows us to recover other optical quantities, such as the absorption coefficient and reflectivity (*Egerton, 1996*). In order to obtain the dielectric function, a first step is to derive the single-scattering distribution from the experimental spectrum. We used FLOG (Fourier-Log Deconvolution) program (*Egerton, 1996)* to calculate this single scattering distribution. Then we ran KRAKRO, a K-K analysis program, to calculate the real part ε_1 and imaginary part ε_2 of the dielectric function. The resulting dielectric function is shown in Figure 4.6(a).

In order to relate electron energy-loss measurements to optical measurements of pentacene thin films, the optical absorption coefficient $\mu(E)$, is the quantity of interest. We calculated μ using the relation between $\mu(E)$ and $\varepsilon(E)$ (*Egerton, 1996*):

$$\mu(E) = (2E/\hbar c)\left\{\frac{1}{2}\left[\left(\varepsilon_1^2 + \varepsilon_2^2\right)^{1/2} - \varepsilon_1\right]\right\}^{1/2}. \quad (4\text{-}1)$$

The $\mu(E)$ retrieved from EELS data is shown in Figure 4.6(b). The peak positions at absorption coefficient maxima are: 3.32, 6.33, 8.46, 12.53 eV. The energy range in EELS is much greater and due to the worse energy resolution of EELS compared to optical spectroscopy, we cannot see many peaks in low energy (0.5 eV – 3 eV) EELS as in UV spectrum. Therefore, we can't compare our data on the positions of the optical absorption coefficient maxima with our UV absorption measurement (Section 4.2).

Reproduced with permission of the copyright owner. Further reproduction prohibited without permission.

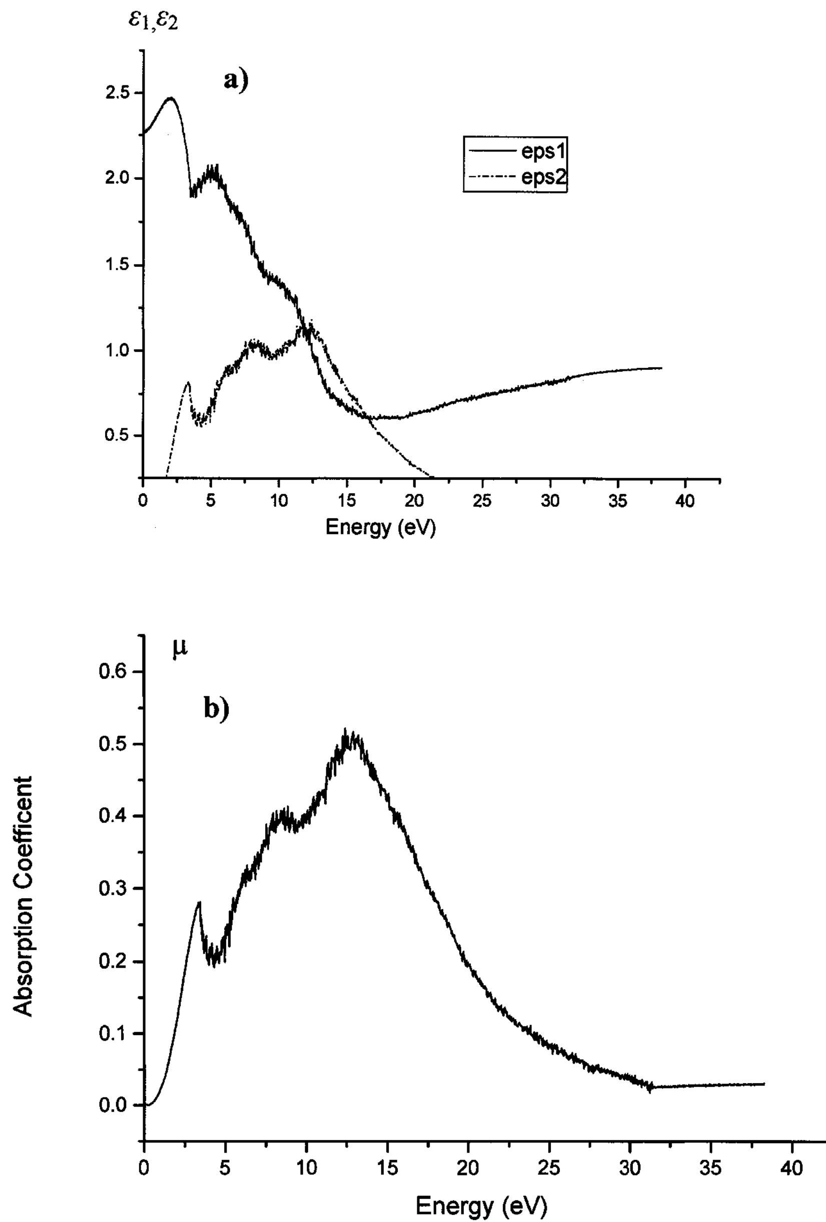

Figure 4.6. a) The dielectric constant ε_1 and ε_2 for pentacene films calculated from the energy loss function; b) the calculated optical absorption coefficient μ (E).

Reproduced with permission of the copyright owner. Further reproduction prohibited without permission.

Chapter 5. Summary

This thesis describes the growth of pentacene thin films by high-vacuum thermal evaporation onto different substrates including amorphous carbon, glass, Si(001) and mica. Pentacene thin films grown on these substrates were characterized by means of TEM, XRD, AFM and optical microscopy techniques.

Pentacene thin films deposited at room temperature or at elevated temperature are polycrystalline and have layered structures. At room temperature only the "thin film phase" films with inter-planar *d*(001) spacing of 15.3 Å were obtained. Whereas, co-existence of two different phases, "thin film phase" with *d*(001) of 15.3 Å and "bulk phase" with *d*(001*) of 14.4 Å, was observed in thin films deposited at elevated temperature. In the latter case, the *ab* planes are parallel to the substrate, and pentacene molecules are standing up and almost perpendicular to the substrate surface.

In order to understand the film formation mechanism, pentacene films with thickness gradient (from sub-monolayer to 70 nm) were obtained using shadow mask or by deposition with constant growth rate and varying deposition time. The evolution of thin film formation was observed and described as four stages: island stage, coalescence stage, channel stage and continuous film formation. During the initial stage, two different shapes of 2D islands (dendritic and smooth edge shaped) were observed. At the lower nucleation density, fractal growth is found to be the preferred growth mode. It is also found that the growth mode transits from 2D to 3D at one monolayer thickness, along with dramatic shape and height changed of the pentacene islands. The crystallographic orientation of pentacene didn't change during this

Reproduced with permission of the copyright owner. Further reproduction prohibited without permission.

transition. It is speculated that the driving force for these transitions is the minimization of surface energy. With the continuation of deposition, the isolated islands grew in 3D mode. Eventually, larger grains with lamellar shape were formed through connecting with neighboring islands.

The effects of growth conditions, such as substrate temperature and thermal evaporation rate, on the morphology and structure of pentacene films were also investigated. Lower evaporation rate implies lower nucleation density and larger grain size. Lateral film crystallite dimensions up to 2 μm were grown on amorphous carbon substrate at a deposition rate of 0.5 Å/s, while less than 0.2 μm was achieved at a deposition rate of 1 Å/s. The substrate temperature was also found to play a crucial role during the deposition of films. The lateral crystallite dimensions up to 40 μm were achieved at a deposition rate of 0.5 Å/s at substrate temperatures of 40 °C and 60 °C. However, two different crystal phases were induced at elevated temperatures, as previously discussed. Thermal annealing of as-deposited pentacene films may remove some defects within the films and recrystallization was observed. However, the annealing conditions, such as annealing time and temperature, failed to provide enough control to obtain continuous, defect-free pentacene thin films.

Vis-UV absorption measurement of pentacene films deposited onto fused quartz at RT was carried out. The Davydov splitting in the absorption spectrum was observed. The splitting is at about 0.1 eV (720 cm^{-1}) corresponding to the singlet state excitation (S_0-S_1). The lowest excited state in the absorption spectrum is 1.85 eV. PL for pentacene films deposited onto Si(001) at RT was also measured.

Reproduced with permission of the copyright owner. Further reproduction prohibited without permission.

The sensitivity of pentacene films to electron beam irradiation in an analytical TEM was investigated at both room temperature and 90 K. Loss of crystallinity and degradation of pentacene molecular structure, as observed by changes in low loss electron energy loss spectroscopy, were used as a measurement of electron radiation damage. The excitation cross sections suggest that the damage mechanism in pentacene is likely related to the carbon K-shell excitation.

In general, we deposited pentacene films at RT and at elevated temperature, characterized the film structure, morphology and optical properties, observed the evolution of films growth and studied their electron beam sensitivity. There are, however, many different directions that can be followed for future research. For example, modeling of the change in film growth modes, the relation between pentacene film morphology and their optical and electrical properties, and the possibility of making microcavity OLED with pentacene are all open fields that can be studied.

Reproduced with permission of the copyright owner. Further reproduction prohibited without permission.

References

Amar, J. G., Family, F. and Lam, P. M., *Physics Review B*, **50**, 8781, (1994).

Bao, Z., *Advanced Materials*, **12**, 227, (2000).

Burroughes, J. H., Bradley, D. D. C., Brown, A. R., Marks, R. N., Mackay, K., Friend, R. H., Burns, P. L. and Holmes, A. B., *Nature*, **347**, 539, (1990).

Burrows, P. E. and Forrest, S. R., *Applied Physics Letters*, **64**, 2285, (1994).

Campbell, R. B., Robertson, J. M., and Trotter, J., *Acta Crystallography*, **14**, 705, (1961).

Chabinyc, M. L. and Salleo, A., *Chemistry of Materials*, **16**, 4509, (2004).

Chen, C., *Chemistry of Materials*, **16**, 4389, (2004).

Davydov, A. S., *Theory of molecular excitons*, Plenum Press, (1971).

Coakley, K. M. and McGehee, M. D., *Chemistry of Materials*, **16**, 4533, (2004).

Dimitrakopoulos, C. D., Brown, A. R. and Pomp, A., *Journal of Applied Physics*, **80**, 2501, (1996).

Dimitrakopoulos, C. D. and Mascaro, D. J., *IBM Journal of Research and Development*, **45**, 11, (2001).

Dimitrakopoulos, C. D. and Malenfant, P. R. L., *Advanced Materials*, **14**, 99, (2002).

Dodabalapur, A., Torsi, L. and Katz, H. E., *Science*, **268**, 270, (1995).

Drummy, L. F., Miska, P. K. and Martin, D. C., *Material Research Society Proceedings*, **734**, (2002).

Egerton, R. F., Li, P. and Malac, M., *Micron*, **35**, 299, (2004).

Egerton, R. F., *Electron Energy Loss Spectroscopy in the Electron Microscope*, 2nd ed., Plenum, (1996).

Forrest, S. R., *IEEE Journal on Selected Topics in Quantum Electronics*, **6**, 1072, (2000).

Forrest, S. R., *Chemical Reviews*, **97**, 1793, (1997).

Reproduced with permission of the copyright owner. Further reproduction prohibited without permission.

Garnier, F., Horowitz, G., Fichou, D. and Yassar, A., *Supramolecular Science,* **4**, 155, (1997).

Glaeser, R. M., in *Physical Aspects of Electron Microscopy & Microbeam Analysis* (Siegel, B. and Beaman, D. R., eds.), John Wiley & Sons, (1975).

Heringdorf, F.-J., Reuter, M. C. and Tromp, R. M., *Nature*, **412,** 517, (2001).

Holmes, D., Kumaraswamy, S., Matzger, A. J., Vollhardt, K. P. C., *Chemistry - A European Journal*, **5**, 3399, (1999).

Hoppe, H. and Sariciftci, N. S., *Journal of Material Research,* **19**, 1924, (2004).

Horowitza, G., *Journal of Material Research,* **19**, 1946, (2004).

Hughes, G., Roche, J., Carty, D., Cafolla, T. and Smith, K. E., *Journal of Vacuum Science and Technology*, **20**, 1620, (2002).

Hunter, E. E., *Practical Electron Microscopy: A Beginner's Illustrated Guide*, Abbey Publishing, (1984).

Jackson, N., Lin, Y. Y. and Gundlach, D. J., *IEEE Journal of Selected Topics on Quantum Electronics*, **4**, 100, (1998).

Karl, N., *Synthetic Metals*, **133-134**, 649, (2003).

Kasaya, M., Tabata, H. and Kawai, T., *Surface Science*, **400**, 367, (1998).

Kelley, T. W., Baude, P. F., Gerlach, C., Ender, D. E., Muyres, D., Haase, M. A., Vogel, D. E. and Theiss, S. D., *Chemistry of Materials*, **16**, 4413, (2004).

Lee, K. O. and Gan, T. T., *Chemical Physics Letters*, **51**,120, (1977).

Lumb, M.D., *Luminescence Spectroscopy*, Academic Press, (1978).

Maissel, L. I. and Glang, R., *Handbook of Thin Film Technology*, McGraw-Hill, (1983).

Mattheus, C. C., Dros, A. B., Baas, J., Oostergetel, G. T., Meetsma, A., Boer, J. L. de and Palstra, T. T. M, *Synthetic Metals*, **138**, 475, (2003).

Möller, S., Perlov, C., Jachson, W., Taussig, C. and Forrest, S. R., *Nature*, **426**, 166, (2003).

Park, S. P., Kim, S. S., Kim, J. H., Whang, C. N. and Im, S., *Applied Physics Letters*, **80**, 2872, (2002).

Pinsker, Z. G., *Electron Diffraction*, Butterworths, London, (1953).

Reproduced with permission of the copyright owner. Further reproduction prohibited without permission.

Reimer, L., *Laboratory Investigation*, **114**, (1965).

Rogers, J. A. and Bao, Z., *Journal of Polymer Science Part A: Polymer Chemistry*, **40**, 3327, (2002).

Ruiz, R., Choudhary, D., Nickel, B., Toccoli, T., Chang, K., Mayer, A. C., Clancy, P., Blakely, J. M., Headrick, R. L., Iannotta, S. and Malliaras, G. G., *Chemistry of Materials*, **16**, 4497, (2004).

Ruiz, R., Nickel, B., Koch, N., Scoles, G., Feldman, L. C., Haglund, R. F. and Kahn, A., *Physics Review B*, **67**, 125406, (2003).

Schoonveld, W. A., *Transistors based on ordered organic semiconductors*, Ph.D thesis, University of Groningen, the Netherland, (1999).

Sheats, J. R., *Journal of Material Research*, **19**, 1974, (2004).

Tang, C. W. and van Slyke, S. A., *Applied Physics Letters*, **51**, 913 (1987).

Turner-Jones, E. T., Chyan, O. M. and Wrighton M. S., *Journal of American Chemical Society*, **109**, 5526, (1987).

Venables, J. A., *Surface Science*, **299/300**, 798, (1994).

Verlaak, S., Steudel, S. and Heremans, P., *Physics Review B*, **68**, 195409, (2003).

Wu, J. S. and Spence, J. C. H., *Journal of Applied Crystallography*, **37**, 78-81, (2004).

Reproduced with permission of the copyright owner. Further reproduction prohibited without permission.

Appendix: Calculation of *d* spacing and ratios of (*hkl*) planes

Crystallographic formula for interplanar spacing of the (*hkl*) plane in triclinic crystal system is

$$\frac{1}{d^2} = \frac{1}{V^2}\left(S_{11}h^2 + S_{22}k^2 + S_{33}l^2 + 2S_{12}hk + 2S_{23}kl + 2S_{33}lh\right),$$

where

$$V^2 = a^2b^2c^2(1 - \cos^2\alpha - \cos^2\beta - \cos^2\gamma + 2\cos\alpha\cos\beta\cos\gamma),$$

and

$$S_{11} = b^2c^2\sin^2\alpha,$$

$$S_{22} = a^2c^2\sin^2\beta,$$

$$S_{33} = a^2b^2\sin^2\gamma,$$

$$S_{12} = abc^2(\cos\alpha\cos\beta - \cos\gamma),$$

$$S_{23} = a^2bc(\cos\beta\cos\gamma - \cos\alpha),$$

$$S_{31} = ab^2c(\cos\lambda\cos\alpha - \cos\beta).$$

(1). Bulk Phase

With the following known lattice parameters for bulk structure of pentacene (*Campbell, 1961*):

$a = 7.93 \pm 0.02$ Å, $b = 6.14 \pm 0.02$ Å, $c = 16.03 \pm 0.05$ Å;

$\alpha = 101.9°$, $\beta = 112.6°$, $\gamma = 85.8°$,

the *d* spacings of given (*hkl*) planes are calculated as below:

Reproduced with permission of the copyright owner. Further reproduction prohibited without permission.

h	k	l	d	Ratio over d(001)	Ratio over d(010)
0	0	1	14.53	1.00	
0	1	0	6.01	0.41	1.00
1	0	0	7.32	0.50	1.22
0	0	2	7.26	0.50	1.21
0	2	0	3.00	0.21	0.50
2	0	0	3.66	0.25	0.61
1	1	0	4.63	0.32	0.77
1	0	1	5.73	0.39	0.95
0	1	1	5.21	0.36	0.87
0	0	3	4.84	0.33	0.81
0	3	0	2.00	0.14	0.33
3	0	0	2.44	0.17	0.41
2	1	0	3.12	0.21	0.52
2	0	1	3.27	0.23	0.54
1	2	0	2.77	0.19	0.46
1	0	2	4.40	0.30	0.73
1	1	1	3.99	0.27	0.66
0	0	4	3.63	0.25	0.60
0	4	0	1.50	0.10	0.25
4	0	0	1.83	0.13	0.30
1	1	2	3.36	0.23	0.56
1	2	1	2.58	0.18	0.43
2	1	1	2.82	0.19	0.47
0	1	3	3.46	0.24	0.58
1	0	3	3.48	0.24	0.58
1	3	0	1.93	0.13	0.32
3	1	0	2.26	0.16	0.38
2	0	2	2.86	0.20	0.48
2	2	0	2.32	0.16	0.39
0	0	5	2.91	0.20	0.48
0	5	0	1.20	0.08	0.20
5	0	0	1.46	0.10	0.24
3	2	0	1.89	0.13	0.31
3	0	2	2.09	0.14	0.35
2	3	0	1.75	0.12	0.29
1	4	0	1.47	0.10	0.24
4	1	0	1.75	0.12	0.29
1	0	4	2.85	0.20	0.47
4	0	1	1.74	0.12	0.29
1	1	3	2.84	0.20	0.47
1	3	1	1.85	0.13	0.31
3	1	1	2.10	0.14	0.35

Reproduced with permission of the copyright owner. Further reproduction prohibited without permission.

(2). Thin Film Phase

With the following known lattice parameters for "thin film phase" structure of pentacene (*Wu, 2004*):

$a = 6.1$ Å, $b = 7.6$ Å, $c = 15.3$ Å,

$\alpha = 81.0°$, $\beta = 85.0°$, $\gamma = 89.5°$,

the d spacings of given (hkl) planes are calculated as below:

h	*k*	*l*	*d*	Ratio over *d*(001)	Ratio over *d*(010)
0	0	1	14.37	1.00	
0	1	0	5.94	0.41	1.00
1	0	0	7.24	0.50	1.22
0	0	2	7.19	0.50	1.21
0	2	0	2.97	0.21	0.50
2	0	0	3.62	0.25	0.61
1	1	0	4.58	0.32	0.77
1	0	1	5.67	0.39	0.95
0	1	1	5.15	0.36	0.87
0	0	3	4.79	0.33	0.81
0	3	0	1.98	0.14	0.33
3	0	0	2.41	0.17	0.41
2	1	0	3.09	0.21	0.52
2	0	1	3.23	0.23	0.54
1	2	0	2.74	0.19	0.46
1	0	2	4.35	0.30	0.73
1	1	1	3.95	0.27	0.66
0	0	4	3.59	0.25	0.60
0	4	0	1.49	0.10	0.25
4	0	0	1.81	0.13	0.30
1	1	2	3.32	0.23	0.56
1	2	1	2.55	0.18	0.43
2	1	1	2.79	0.19	0.47
0	1	3	3.42	0.24	0.58
1	0	3	3.44	0.24	0.58
1	3	0	1.91	0.13	0.32
3	1	0	2.23	0.16	0.38
2	0	2	2.83	0.20	0.48
2	2	0	2.29	0.16	0.39
0	0	5	2.87	0.20	0.48
0	5	0	1.19	0.08	0.20

Reproduced with permission of the copyright owner. Further reproduction prohibited without permission.

5	0	0	1.45	0.10	0.24
3	2	0	1.87	0.13	0.31
3	0	2	2.07	0.14	0.35
2	3	0	1.73	0.12	0.29
1	4	0	1.45	0.10	0.24
4	1	0	1.73	0.12	0.29
1	0	4	2.82	0.20	0.48
4	0	1	1.72	0.12	0.29
1	1	3	2.81	0.20	0.47
1	3	1	1.83	0.13	0.31
3	1	1	2.08	0.14	0.35

Reproduced with permission of the copyright owner. Further reproduction prohibited without permission.